Interface-Driven Electrocatalysis: Highlighting the Role of $NdNiO_3$-NiO Heterointerface in Urea Electro-oxidation

Nikhil N. Rao [1,2]#, Chandraraj Alex [1,3]#, Shalini Tomar [4], Muhammed Safeer N. K. [1], Seung-Cheol Lee [4,5], Satadeep Bhattacharjee [4], Neena S. John [1]*

[1] *Centre for Nano and Soft Matter Sciences, Shivanapura, Bengaluru 562162, India*

[2] *Manipal Academy of Higher Education, Manipal 576104, India.*

[3] *Institute of Inorganic Chemistry, Kiel University, Otto-Hahn-Platz 10, 24118 Kiel, Germany*

[4] *Indo-Korea Science and Technology Center (IKST), Bangalore 560064, India*

[5] *Electronic Materials Research Center, Korea Institute of Science and Technology, Korea*

*Corresponding author Email: jsneena@cens.res.in

#*Equal contribution*

Abstract:

Enhancing the activity of Ni-based catalysts for the electrochemical urea oxidation reaction (UOR) through the construction of heterojunctions or by heteroatom doping primarily involves the generation of polarized and/or high-valent Ni sites. However, systematic investigations of the impact of this strategy on the formation of UOR-active NiOOH species and its influence on UOR activity are scarce. Herein, we have chosen $NdNiO_3$-NiO catalysts to systematically vary the average oxidation of Ni from +2 to +3 by adjusting the stoichiometric ratio of $NdNiO_3$ to NiO. Detailed electrochemical analysis and *in situ* X-ray absorption spectroscopy have revealed that the catalyst systems rich in $NdNiO_3$-NiO heterointerfaces exhibit more favourable formation of NiOOH species and, subsequently, better UOR activity. Interestingly, this enhanced UOR activity does not show an obvious positive correlation with the increase in the average oxidation state of Ni. The UOR current density follows the trend NNO2NO8 (20% $NdNiO_3$ and 80% NiO) > NNO8NO2 > NNO6NO4 > NNO4NO6 > NiO > $NdNiO_3$. The higher UOR activity of NNO2NO8 and NNO8NO2 is attributed to the more effective formation of surface-exposed heterointerfaces, thereby establishing the dependence of UOR activity on these active heterointerfaces. *In situ* Raman spectroscopy substantiates the formation and sustained presence of NiOOH in $NdNiO_3$-NiO heterointerface during UOR. Theoretical studies reveal that modulation of electronic structure through charge redistribution at the heterointerface optimizes hydroxylation, urea adsorption, and CO_2 desorption, consequently leading to enhanced UOR performance. These insights bring attention to the importance of heterointerface engineering in enhancing Ni-based UOR electrocatalysts.

Keywords: heterointerface, $NdNiO_3$-NiO, *in situ* X-ray absorption spectroscopy, NiOOH species, urea electro-oxidation, *in situ* Raman spectroscopy

1. Introduction

The conventional water splitting reaction for generating the sustainable and clean fuel, H_2, comprises the cathodic-hydrogen evolution reaction (HER) and the anodic-oxygen evolution reaction (OER) [1]. The high energy input demanded by OER is addressed by replacing it with alternative oxidation reactions, such as urea oxidation, ethanol oxidation, methanol oxidation, furfural oxidation, etc. [2], which can operate at a thermodynamically lower overpotential than OER. Electrochemical urea oxidation reaction (UOR) has several advantages, such as the high solubility of urea in water and abundant availability of the molecule as metabolic wastes from animals, run-off from agricultural fields, industrial wastewater, etc. [3]. Thus, UOR also remediates the ill effects of excess urea by converting it into N_2 and dissolved CO_3^{2-} in alkaline solution [4], thereby endowing a wastewater treatment functionality to this technology. Nevertheless, UOR involves a $6e^-$ transfer process and suffers from poor kinetics, and the UOR catalysts face challenges such as loss of active sites and their deactivation by CO_x poisons during prolonged electrolysis. Ni-based catalysts are widely demonstrated as efficient UOR catalysts [5], due to the favourable intermediate adsorption characteristics of the active NiOOH species that are formed on the surface of these catalysts on electrochemical activation in alkaline media [6].

Construction of hierarchal nanostructures, active phase engineering, defect engineering, improving the oxidation state of Ni, heteroatom incorporation, construction of heterointerfaces/heterojunctions, etc., are some of the widely employed strategies to boost the UOR activity of Ni-based catalysts [7,8]. The incorporation of heteroatoms could help achieve rational modulation of electronic structures of Ni-based UOR catalysts by facilitating the charge transfer behaviour and enhancing the intrinsic reactivity of the catalysts toward the formation of active species [8,9]. In Ru-doped $Ni(OH)_2$, anchored atomic Ru sites are shown to regulate the charge transfer by redistributing the charge density of metal sites, leading to enhanced UOR activity [10]. Ce-doping in α-$Ni(OH)_2$ is shown to result in a polarizing function strengthening the electropositive behaviour of Ni centers, thereby boosting the UOR activity of high-valence Ni species [11]. Similarly, accelerated electron transport and a downshift of the *d*-band centre of β-$Ni(OH)_2$ are reported to give rise to high UOR activity in La-doped β-$Ni(OH)_2$ [12]. In $Ni_{0.99}Co_{0.01}(OH)_2$, it is shown that Co-doping enhances the proportion of UOR-active Ni^{3+} ions through the creation of Ni cation defects, thereby enabling defect-engineering in α-$Ni(OH)_2$, subsequently giving rise to enhanced UOR activity [13]. Qiuhan Cao *et al.* have reported optimized UOR activity in the $V_{10\%}$-Ni_5P_4 system by gradual V-doping and proposed that V-doping aids in tuning the electronic structure of the catalysts, resulting in abundant formation of active -NiOOH species [14]. Similarly, the incorporation of other transition metal ions, such as Mo [15], Cr [16],

Cu [17], Fe [18], Mn [19], W [20], etc., are shown to enhance the formation of active, high-valent Ni-species that are essential for efficient UOR electrocatalytic activity.

Heterojunction catalysts have also gained immense importance in the field of electrocatalysis mainly because (a) the lattice strain induced in a heterojunction interface could expose an abundant number of active sites, (b) the charge transfer and local charge redistribution between the components through synergy can promote the electrocatalytic activity [21–23]. Co_2P–Ni_3S_2 heterostructured nanocrystals have exhibited high UOR output due to an enhancement in the number of active Ni^{3+} centers resulting from the electron transfer between Ni_3S_2 and Co_2P at the heterostructured interface [24]. A crystalline–amorphous Ni_3S_2–$NiMoO_4$ heterostructure has been developed as a bifunctional - UOR and HER catalyst, which harbours a regulated interfacial electronic structure through the synergic electron transfer from Ni_3S_2 to $NiMoO_4$, resulting in an escalated formation of NiOOH species [25]. $Ni_2P_4O_{12}$/NiTe heterojunction catalyst exhibits dynamic generation of Ni^{3+} active sites through a novel Ni^{3+}/Ni^{2+}-mediated pathway, which effectively oxidizes urea and desorbs CO_2, thereby proving to be a superior UOR electrocatalyst [26]. Ni_3S_2–Ni_3P heterostructure exhibits appreciable UOR activity due to the existence of two kinds of $Ni^{\delta+}$ with different coordination environments [27]. Ping Gao and team have developed NiF_3/Ni_2P heterojunction wherein the flow of electrons from Ni_2P to NiF_3 through the interface facilitates increased generation of Ni^{3+} ions and induces a local charge density redistribution at the interface enhancing the urea binding characteristics [28]. Recent studies have shown that surface reconstruction in $NiSe_2$/$MoSe_2$ Mott-Schottky heterojunction forms a Mo-NiOOH/$NiSe_2$ composite, enhancing UOR activity by optimizing intermediate adsorption/desorption [29]. Similarly, Fe-doping in a Ni_3S_2@$NiSe_2$ heterojunction boosts UOR activity by forming Fe-NiOOH active species, which lowers energy barriers for UOR [30]. In another recent investigation, Haoran Ding et al. investigated $LaNiO_3$-NiO heterostructure as an electrocatalyst for UOR [22] and shown that the built-in electric fields induced by the flow of electrons from the $LaNiO_3$ to the NiO phase facilitate the adsorption of urea molecules, imparting superior UOR activity to the catalyst. However, the influence of the heterointerface on the formation and stabilization of NiOOH-active species, as well as the effect of sequentially tuning the ratios of the constituent phases on the oxidation state of Ni and the UOR activity of the catalyst, has not yet been investigated.

In an earlier study, N N Rao *et al.* have shown that the rare earth metal nickelate – $NdNiO_3$, due to the presence of inherently stabilized Ni^{3+} ions, exhibits superior UOR activity and operates via the direct mechanism, while Ni^{2+}-rich NiO prefers the indirect mechanism of UOR [31]. Hence, we have chosen a $NdNiO_3$-NiO catalyst system to gain insights into the influence of heterointerfaces and average oxidation states of Ni sites on the electrocatalytic activity of Ni-based UOR catalysts. The adopted chemical synthesis route involving coprecipitation wherein both $NdNiO_3$ and NiO are formed simultaneously facilitates the

abundant generation of heterointerfaces with intimate contact. The formation of heterointerfaces in $NdNiO_3$-NiO catalysts is examined using electron microscopy and energy-dispersive X-ray analysis. The average oxidation state of Ni in the $NdNiO_3$-NiO catalysts can be tuned between Ni^{2+} and Ni^{3+} by systematically varying the ratio of NiO to $NdNiO_3$ as monitored by X-ray absorption near edge structure (XANES) and X-ray photoelectron spectroscopy (XPS). This system provides an ideal platform to explore the UOR activity of such catalyst systems and its correlation with the role of the heterointerface and the average oxidation state of Ni. Electrochemical studies have revealed that the $NdNiO_3$-NiO catalysts containing 20% of $NdNiO_3$ - 80% NiO and 80% $NdNiO_3$ - 20% NiO exhibit more feasible formation of NiOOH species, high UOR mass activity, and low Tafel slope. *In situ* X-ray absorption spectroscopy and electrochemical impedance spectroscopy are utilized to understand the changes in the average oxidation state and ascertain the mechanism of UOR operating in $NdNiO_3$-NiO catalyst systems. Theoretical calculations using density functional theory (DFT) are also performed to derive the free energy diagram of the typical UOR pathway, evaluate the adsorption energies of the reactants – hydroxyl ions and urea molecules and the product CO_2 at the heterointerface of $NdNiO_3$-NiO, corroborating the experimental results. This study has demonstrated that the influence of the properties of the heterointerface dominates over the influence of the average oxidation state of Ni in determining the UOR activity of the catalyst.

2. Experimental section

2.1. Synthesis of $NdNiO_3$-NiO catalyst systems

$NdNiO_3$-NiO catalysts were synthesized by annealing the co-precipitated mixed hydroxides of Ni and Nd in a flowing oxygen atmosphere. The strategy employed is to take a measured excess of the Ni-precursor such that equal moles of Nd and Ni react to form $NdNiO_3$ under the reaction conditions, while the excess Ni precursor forms NiO, thereby generating catalysts containing different relative amounts of $NdNiO_3$ and NiO phases, with the formation of $NdNiO_3$-NiO heterointerfaces between them. Nickel (II) chloride hexahydrate (99%, Merck) and neodymium (III) acetate hydrate (99.9%, Sigma-Aldrich) were used as the metal precursors. $Nd(CH_3CO_2)_3$ and $NiCl_2.6H_2O$ were taken in the molar ratios: 1:1, 0.8:1, 0.6:1, 0.4:1, 0.2:1, 0:1, dissolved in deionized water separately and mixed under vigorous stirring for 30 min at room temperature. A 0.50 M sodium hydroxide solution (99.99%, Sigma-Aldrich) was added dropwise to the mixture and stirred continuously to form Ni-Nd hydroxide gel. After thoroughly rinsing the gel several times with water and ethanol, it was dried in a hot air oven and finely ground into a fine greenish powder using an agate mortar and pestle. The powder was taken in an alumina crucible and subjected to annealing at 800 ^oC with a ramping rate of 5 ^oC per minute in a flowing oxygen atmosphere (99.9%) for 16 hours in a tube furnace. The samples obtained from the Nd:Ni precursor ratios of 1:1, 0.8:1, 0.6:1, 0.4:1, 0.2:1, 0:1 are labelled as $NdNiO_3$, NNO8NO2, NNO6NO4, NNO4NO6, NNO2NO8, and NiO, respectively (NNO

stands for $NdNiO_3$ and NO stands for NiO).

2.2. Material characterization

The crystal structure of the catalysts was studied by powder X-ray diffraction (XRD) patterns obtained from a Rigaku SmartLab X-ray diffractometer using Cu Kα radiation (λ = 1.5406 Å) in the Bragg-Brentano focusing mode with θ increment of 1.2°/min. High-resolution surface images of the catalysts were obtained from TESCAN MIRA3 LMU field emission scanning electron microscope (FESEM). Energy dispersive spectroscopy (EDS) was performed by Quantax 200 using a Peltier-cooled silicon drift detector system integrated with the FESEM to ascertain the composition of elements in the synthesized catalysts. Transmission electron microscopy (TEM) images were captured using a Thermo Scientific Talos F200S G2 TEM instrument. X-ray photoelectron spectroscopy (XPS) measurements were performed using Thermofisher K-Alpha with Al Kα micro-focused monochromator with variable spot size, hemispherical analyzer with 128-channel detector, and dual beam charge neutralization. Inductively-coupled plasma optical emission spectroscopy (ICP-OES) was performed using Thermo Scientific Duo iCAP 6000 series to accurately determine the loading amount of Ni (Refer Table S2) on the working electrode. *In-situ* Raman spectra were acquired using a custom-made acrylate spectroelectrochemical cell using Horiba Jobin Yvon XploRA PLUS V1.2 MULTILINE (532 nm laser with 50 X, laser power of 6.25 mW, accumulation of 2 cycles and acquisition time of 60 s). X-ray absorption near edge spectroscopy (XANES) experiments at room temperature (298 K) were performed at PETRA III, P64 beamline of Deutsches Elektronen-Synchrotron (DESY), Germany [32]. Monochromatic X-rays were obtained using a Si (111) double crystal monochromator, which was calibrated using Ni foil (8333 eV). XANES spectra of Ni-K edge from the catalysts were acquired in the fluorescence mode using a passivated implanted planar silicon (PIPS) detector.

2.3. Electrochemical characterization

All electrochemical studies were carried out using a CH760 electrochemical workstation on a glassy carbon electrode (GCE), with Pt wire as the counter and Hg/HgO as the reference electrode. 2 mg of the catalyst was dispersed in a solution containing 200 µL of *N, N*-dimethylformamide (≥99.9%, Sigma-Aldrich) and 50 µL (2 wt%) Nafion (Sigma-Aldrich) solution by sonication for 30 minutes to obtain a homogeneous catalyst ink. 5 µL of the ink was drop-cast on to a well-polished, clean glassy carbon electrode (GCE) of surface area 0.07 cm^2 and used as the working electrode (catalyst mass loading of 40 µg). Cyclic voltammetry (CV) was performed at various scan rates in the potential window of 0 to +0.7 V vs. Hg/HgO in urea– KOH solutions as the electrolyte. The concentrations of urea (ACS reagent, Sigma Aldrich) in 1 M KOH (ACS reagent, Sigma Aldrich) are varied for each catalyst to obtain the optimum concentration for the best activity in terms of maximum current density. Rotating ring disk electrode (RRDE) measurement

was performed in 1 M KOH and 1 M KOH electrolyte containing 0.80 M urea at a rotation speed of 1600 rpm, at a scan rate of 5 mV/s. The ring potential of the Pt ring electrode is fixed at a potential of −0.50 V vs Hg/HgO, which is sufficient to reduce the O_2 evolved at the disk through the oxygen reduction reaction (ORR). In the case of step voltage analysis, the potential was stepped from 0.44 to 0.70 V vs. Hg/HgO in the absence and presence of 0.80 M urea, and the catalyst was held at each potential (40 mV interval) for 60 s. For stability studies, the catalyst was coated on an L-shaped glassy carbon electrode (three-electrode configuration and Ni foam (two-electrode configuration) as the anode in 0.80 M U + 1 M KOH electrolyte. Electrochemical impedance spectroscopy (EIS) was performed in a frequency range of $10^{4.5}$ to 10^{-2} Hz with the amplitude of the sinusoidal wave set to ±5 mV. The electrochemical stability of the catalyst was studied by performing a chronoamperometric test at a specific potential.

In situ XANES and *in situ* Raman measurements were conducted after obtaining a steady current at the desired potential. A custom-made acrylate-based, spectro-electrochemical cell fitted with a Kapton window that is transparent to X-rays was employed. The catalyst-coated carbon fiber paper was positioned close to the window (ca. 0.2 mm distance) to minimize the electrolyte volume between the Kapton window and the catalyst surface that served as the working electrode. Hg/HgO electrode and Pt wire were used as the reference and counter electrodes, respectively, in an electrolyte containing 0.80 M U (molar concentration of urea) and 1 M KOH. ATHENA software was used to perform background subtraction, normalization, and alignment of XANES data, in addition to linear combination fitting (LCF) of XANES spectra.

3. Results and discussion

3.1. Physical characterization

In the synthesis strategy, equal moles of Nd and Ni precursors react to form $NdNiO_3$, while the measured excess of Ni precursor forms NiO. For instance, when 1 mmol of $NiCl_2.6H_2O$ and 0.2 mmol of $Nd(CH_3CO_2)_3$ are used, 0.2 mmol of the Nd precursor and 0.2 mmol of Ni precursor under the given conditions react to form 0.2 mmol of $NdNiO_3$. The remaining 0.8 mmol of Ni precursor forms 0.8 mmol of NiO. Therefore, 1 mmol of Ni precursor and 0.2 mmol of Nd precursor react to form the $NdNiO_3$-NiO catalyst in the component ratio 2:8. Hence, the NiO content can be tuned by varying the amount of Nd precursor used during synthesis. This synthesis strategy yields a series of samples containing both the $NdNiO_3$ and NiO phases in different ratios. The samples obtained from the Nd:Ni precursor ratios of 1:1, 0.8:1, 0.6:1, 0.4:1, 0.2:1, 0:1 are labelled as $NdNiO_3$, NNO8NO2, NNO6NO4, NNO4NO6, NNO2NO8, and NiO, respectively (NNO stands for $NdNiO_3$ and NO stands for NiO). The powder XRD patterns of as-synthesized $NdNiO_3$, NiO and the various $NdNiO_3$-NiO systems are given in Figure 1(a). The XRD pattern of the as-synthesized $NdNiO_3$ shows major peaks at 2θ values of 23.3°, 33.1°, 41°, 43.4°, 47.6°, 49.3°, 53.8°, 55.2°, 59.3°, 69.7°, 74.6° and 79.4° corresponding to (110), (112), (202), (113), (220), (221), (222), (311), (312), (224), (314) and (240) planes, respectively of the orthorhombic structure of $NdNiO_3$ with

Pbnm space group (JCPDS no. 01-080-1947). The XRD pattern of as-synthesized NiO is in perfect agreement with that of face-centered cubic NiO (JCPDS no. 01-075-0269) showing major peaks at 2θ values of 37.2°, 43.4°, 63°, 75.4° and 79.3° indexed to (111), (200), (220), (311) and (222) planes, respectively (Figure 1(a)). The XRD patterns of the various $NdNiO_3$-NiO catalysts show all the peaks corresponding to $NdNiO_3$ as well as NiO (Figure 1(a) and Figure S1). However, with a decrease in the amount of Nd precursor, the intensity of peaks corresponding to $NdNiO_3$ dampens, while the intensity of peaks corresponding to NiO increases relative to the $NdNiO_3$ peaks, from NNO8NO2, NNO6NO4, NNO4NO6, to NNO2NO8.

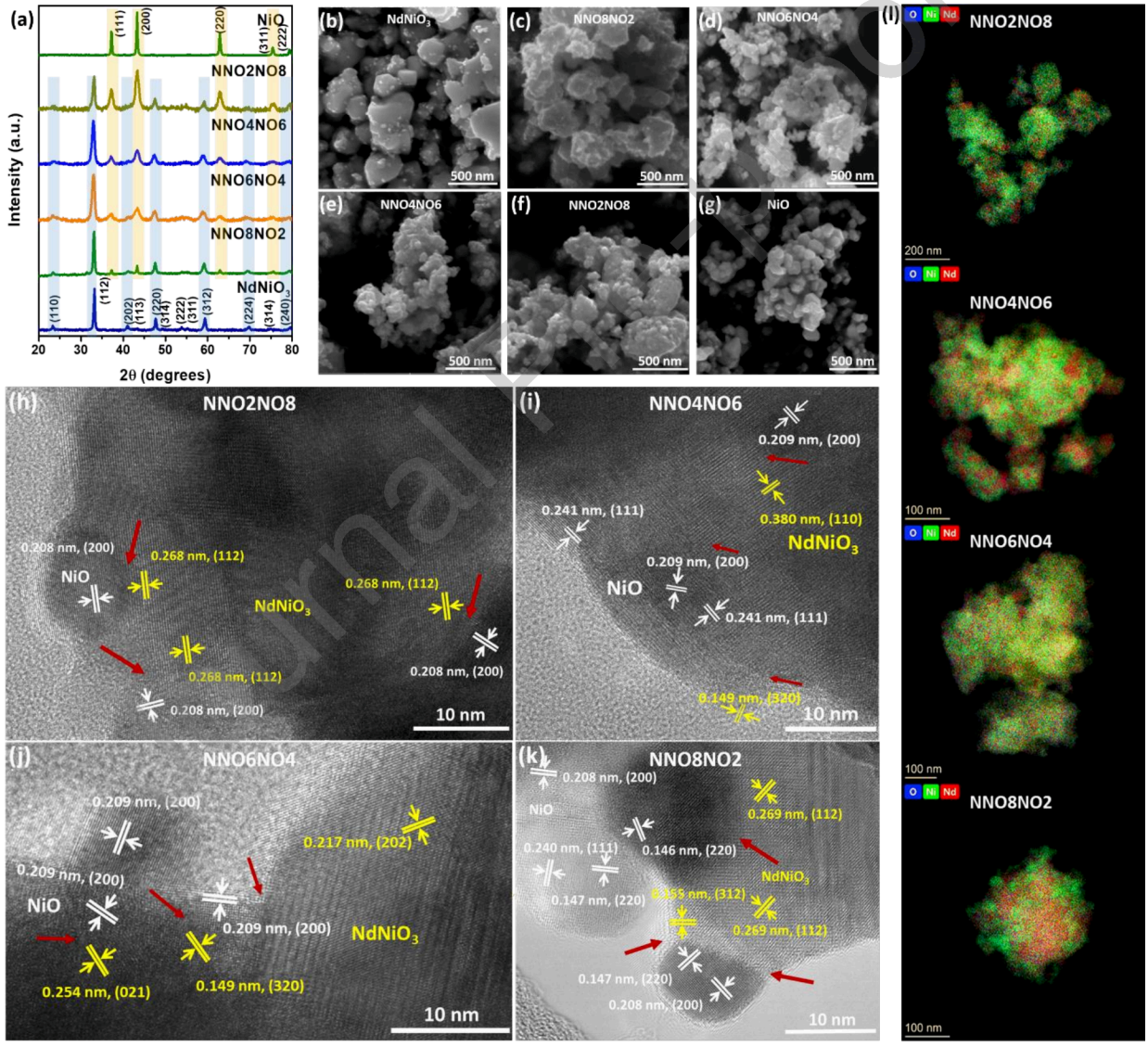

Figure 1. *(a) XRD patterns of $NdNiO_3$, NiO and $NdNiO_3$-NiO catalysts, (b-g) FESEM micrographs of $NdNiO_3$, NiO and $NdNiO_3$-NiO catalysts, (h-k) HRTEM micrographs of $NdNiO_3$-NiO catalysts showing heterointerfaces (l) TEM-EDS elemental mapping composite images of Nd L (red), O K (blue) Ni K (green) in $NdNiO_3$-NiO catalysts.*

FESEM images reveal that $NdNiO_3$ appears to possess flat crystallites, while NiO shows smaller crystallites, and NNO8NO2, NNO6NO4, NNO4NO6, and NNO2NO8 exhibit a mixture of both morphologies (Figure 1(b -g). The HRTEM images of the $NdNiO_3$-NiO catalysts reveal lattice fringes for both $NdNiO_3$ and NiO, corresponding to various crystallographic planes (Figure 1(h-k)). Importantly, the TEM images clearly illustrate the heterointerfaces formed between the *in situ* grown $NdNiO_3$-NiO phases (indicated by red arrows in Figure 1(h-k). For more clarity, the interface regions are marked in the HRTEM images provided in Figure S2. TEM elemental mapping allows us to visualize the distribution of Nd, Ni, and O in the $NdNiO_3$-NiO catalysts (Figure 1(l)). It can be noticed that the X-ray line intensities corresponding to Nd (red) and Ni (green) observed on the various $NdNiO_3$-NiO systems are in accordance with the ratio of both components. TEM-EDS mapping image of NNO2NO8 shows that a smaller number of crystallites consisting of Nd, Ni, and O are formed on larger aggregates consisting of Ni and O. In other words, the smaller aggregates of $NdNiO_3$ are seen distributed all over NiO crystallite aggregates, which could lead to a larger number of surface exposed heterointerfaces in NNO2NO8. Similarly, in the case of NNO8NO2, a smaller number of crystallite aggregates consisting of Ni and O are formed on larger aggregates consisting of Nd, Ni and O, i.e. NiO crystallites are distributed on $NdNiO_3$. In both cases (NNO2NO8 and NNO8NO2), the abundance of heterointerfaces will be more likely due to the minor phase (NiO or $NdNiO_3$) being decorated on the major counterpart phase ($NdNiO_3$ or NiO) when compared to that of NNO4NO6 and NNO6NO4.

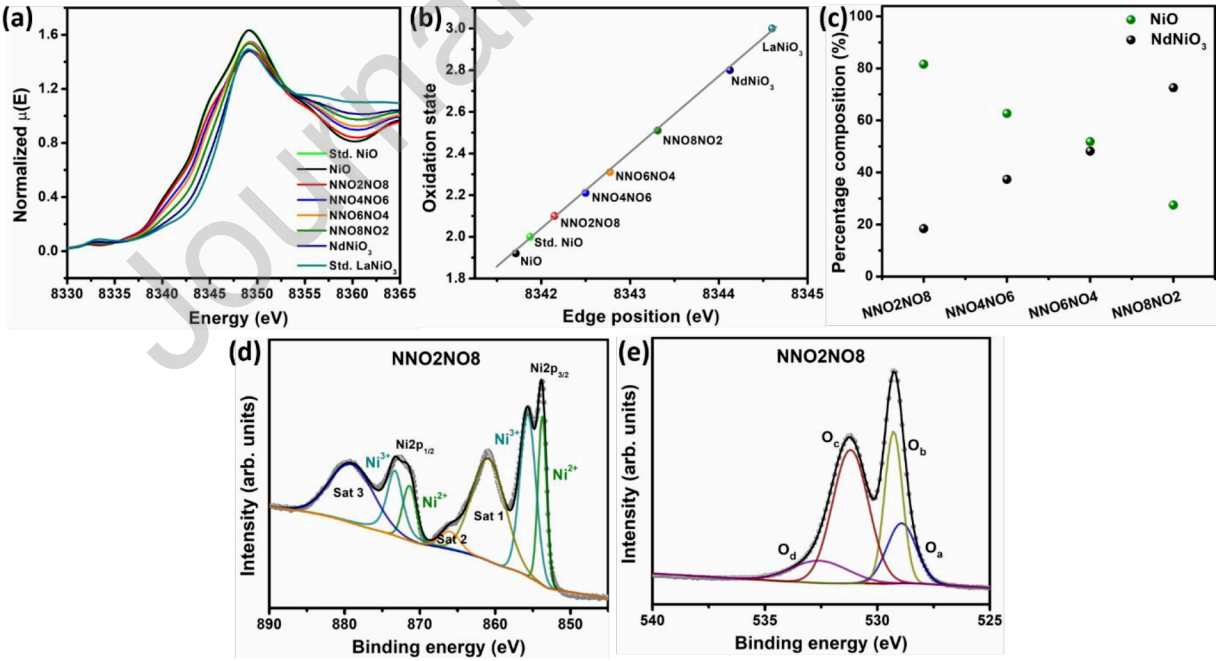

Figure 2. *(a) Ni-K edge XANES plot of as-synthesized $NdNiO_3$-NiO and standards, (b) Calibration plot of Ni oxidation states calculated from Ni-K edge position, (c) Relative percentages of $NdNiO_3$ and NiO in the*

$NdNiO_3$-NiO catalysts from linear combination fitting of XANES spectra, (d) High-resolution Ni2p XPS spectra of NNO2NO8, (e) High-resolution O1s XPS spectra of NNO2NO8.

X-ray absorption spectroscopy has been performed to understand the average oxidation state and the relative composition of different components in the synthesized catalysts. The Ni K-edge XANES spectra of as-synthesized $NdNiO_3$-NiO, and reference compounds, NiO and $LaNiO_3$, are presented in Figure 2(a). The position of the absorption edge is extremely sensitive to the oxidation state of the absorbing atom [23,33]. The edge position is calculated using the integral method (Figure S3), and the oxidation states of the synthesized catalysts are determined from a calibration plot obtained using reference compounds of known oxidation states – NiO (Ni^{2+}) and $LaNiO_3$ (Ni^{3+}) (Figure 2(b)). It is interesting to note from Figure 2(b) that the average oxidation state of Ni increases gradually from NiO (+1.92), NNO2NO8 (+2.10), NNO4NO6 (+2.21), NNO6NO4 (+2.31), NNO8NO2 (+2.51) and $NdNiO_3$ (+2.80), as expected from the increasing content of the Ni^{3+}-rich $NdNiO_3$ phase. The percentage composition of $NdNiO_3$ and NiO in the synthesized catalysts is calculated by performing linear combination fitting (LCF) of their respective XANES spectra (Figure S4) with that of the pure components, $NdNiO_3$ and NiO and is shown in Figure 2(c). The percentage of $NdNiO_3$ increases gradually from 18.40% (± 0.40%) for NNO2NO8 to 72.55% (± 0.50%) for NNO8NO2, while the percentage of NiO decreases from 81.60% (± 1.33%) to 27.45% (± 0.50%) in accordance with the ratios employed during synthesis.

The XPS spectra of the representative sample, NNO2NO8 are presented in Figure 2(d,e) and the Ni2p spectra of the other samples in the series are presented in Figure S5. The Ni2p spectra of NNO2NO8 show peaks at 853.7 and 871.2 eV, corresponding to $Ni2p_{3/2}$ and $Ni2p_{1/2}$ of Ni^{2+}, and peaks at 855.4 and 873.0 eV corresponding to Ni $2p_{3/2}$ and Ni $2p_{1/2}$ of Ni^{3+} (Figure 2(d)) [34]. The characteristic satellite peaks are observed at 860.9, 865.1, and 879.2 eV, respectively. The Ni^{3+}/Ni^{2+}intensity ratio of all the synthesized catalysts is estimated and presented in Figure S5(f). Evidently, the Ni^{3+}/Ni^{2+} intensity ratio increases gradually with an increase in the $NdNiO_3$ content, aligned with the trend in average Ni oxidation states obtained from XANES analysis. Figure 2(e) shows the high-resolution O 1s spectra of NNO2NO8. The deconvoluted O 1s spectra of NNO2NO8 display characteristic peaks at 528.9 eV (O_a) corresponding to the lattice oxide bonded to A-site metal ion, 529.3 eV (O_b) corresponding to the lattice oxide bonded to Ni in $NdNiO_3$, 531.2 eV (O_c) corresponding to surface adsorbed oxygen of defective sites caused by Ni-deficient NiO or Ni^{3+} species, or hydroxide of surface $Ni(OH)_2$ species, and 532.6 eV (O_d) arising from adsorbed water [35,36].

3.2. Electrochemical UOR studies

All the catalysts are subjected to 500 cycles of CV in the same potential window (0.0 V to 0.70 V vs. Hg/HgO) at a scan rate of 100 mV/s for activation of the catalyst surface until no further improvement of

redox current is observed (Figure S6). This activation process facilitates the formation of NiOOH species, which serve as active species for UOR [31,37]. Figure 3(a) displays the CVs of all the $NdNiO_3$-NiO catalysts, along with their pristine components in 1 M KOH at a scan rate of 10 mV/s. In 1 M KOH, the anodic peak (A_1) above 0.44 V vs. Hg/HgO represents the oxidation of Ni^{2+} to Ni^{3+} (formation of NiOOH), while the cathodic peak (C_1) in the reverse scan depicts the reduction of Ni^{3+} to Ni^{2+}. In the forward scan, beyond a potential of 0.65 V vs. Hg/HgO, OER occurs, which is manifested by an increasing anodic current. The area under the oxidation peak in the CV recorded in 1 M KOH, is directly proportional to the number of NiOOH formed on the surface of the catalyst [10]. Figure 3(b) provides the number of NiOOH formed in all the catalysts as estimated from the anodic curve (details in Figure S7 and Table S1) and reveals that the number of NiOOH species furnished by NiO and $NdNiO_3$ is much lower than that of the $NdNiO_3$-NiO catalysts. This indicates that the heterointerfaces that are formed between $NdNiO_3$ and NiO in the $NdNiO_3$-NiO catalysts facilitate the efficient generation of the active species in comparison to the individual components. Among the various $NdNiO_3$-NiO catalysts with different compositional ratios, NNO2NO8 and NNO8NO2 show the highest number of NiOOH species on the surface of the electrode after electrochemical activation and, accordingly, can generate NiOOH species more effectively. Hence, higher UOR activity is expected in the case of NNO2NO8 and NNO8NO2.

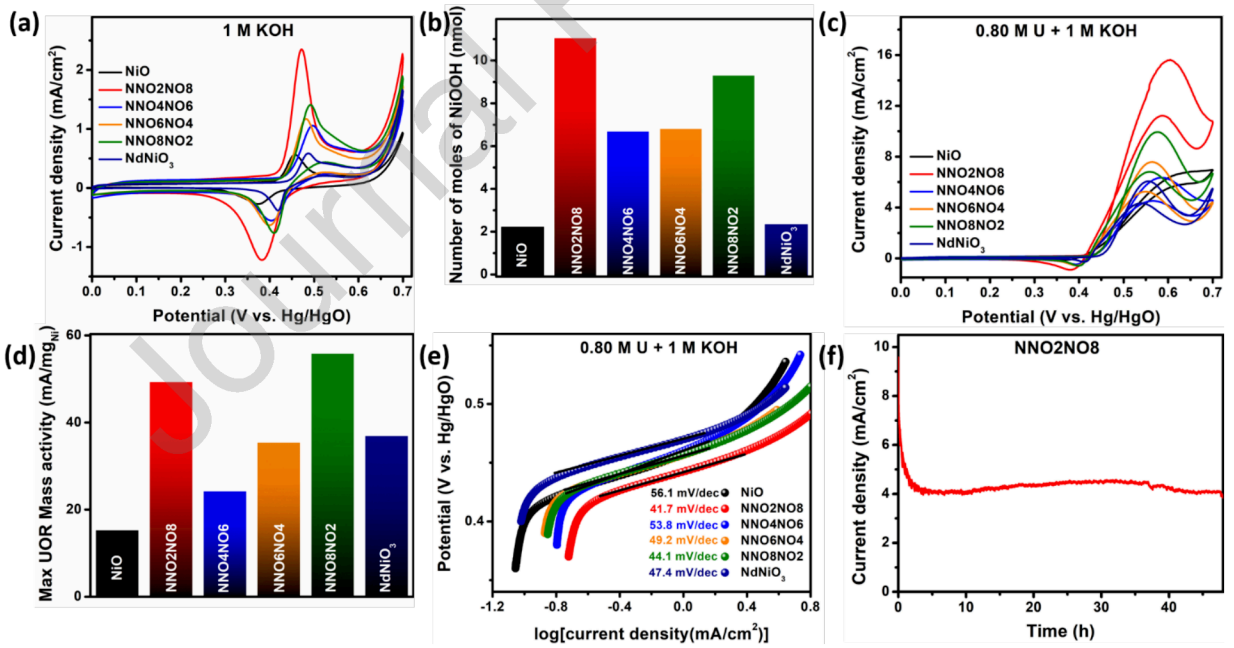

Figure 3. *(a) CVs of all the synthesized catalysts, $NdNiO_3$-NiO in 1 M KOH acquired at a scan rate of 10 mV/s, (b) Comparison of the number of NiOOH species furnished by each catalyst, (c) CVs of all the synthesized catalysts in 0.80 M U + 1 M KOH acquired at a scan rate of 10 mV/s, (d) Maximum UOR mass activity (per mg of Ni) in 0.80 M U + 1 M KOH, (e) Tafel plots of $NdNiO_3$-NiO catalysts in 0.80 M U + 1 M KOH, (f) Chronoamperometric stability test of NNO2NO8.*

Figure 3(c) shows the CVs of $NdNiO_3$-NiO catalysts in 1 M KOH containing 0.80 M urea (1 M KOH + 0.80 M U) at a scan rate of 10 mV/s. In the forward anodic sweep, there is a dramatically enhanced anodic current due to the occurrence of UOR. The anodic UOR peak coincides with the Ni^{2+}/Ni^{3+} oxidation peak, which proves that the Ni^{2+}/Ni^{3+} oxidation (formation of NiOOH) is crucial to enable UOR electrocatalysis [6]. It is also evident that the UOR occurs at a potential that is lower than that required for OER. The anodic peak that is observed in the reverse scan can be attributed to the oxidation of un-oxidized or partially oxidized adsorbed intermediates formed during the forward scan that now undergo complete oxidation at favourable potentials in the reverse scan [38]. As expected from the number of NiOOH sites furnished, NNO2NO8 and NNO8NO2 show enhanced UOR current density compared to the other catalysts, with the peak UOR current density of the former being higher than that of the latter. While the current densities of NNO4NO6 and NNO6NO4 remain smaller than NNO2NO8 and NNO8NO2, they exhibit peak UOR current densities at a lower potential than that of NiO probably due to better electron transport provided by the $NdNiO_3$ component. The CVs recorded in 0.80 M U + 1 M KOH with applied potential in RHE scale is given in Figure S8(a). Since the mass of Ni loaded in each of these catalysts is not the same, it is meaningful to compare their mass activities per mg of Ni, which is calculated by normalizing their peak UOR currents with the mass of Ni loaded, as calculated from ICP-OES analysis (Figure 3(d), Figure S8(b) and Table S2). The mass activity (per mg of Ni) of the catalysts towards UOR follows the trend, NNO8NO2 > NNO2NO8 > $NdNiO_3$ ~ NNO6NO4 > NNO4NO6 > NiO, which also highlights the higher UOR activity of the NNO8NO2 and NNO2NO8 when compared to the other synthesized catalysts. Observably, the trend in UOR activity, which is a function of the amount of NiOOH formed, does not bear any correlation with the increase in the average oxidation state of Ni, as determined by XANES analysis and the Ni^{3+}/Ni^{2+} ratio from XPS peak deconvolution. This suggests that UOR activity is not directly related to the average oxidation state of Ni in the synthesized catalysts. Instead, the differences in UOR activity among the $NdNiO_3$-NiO catalysts could be attributed to the greater number of electrocatalytically active $NdNiO_3$-NiO heterointerfaces present in NNO2NO8 and NNO8NO2.

The variation in UOR activity at different urea concentrations is shown in Figure S9. The optimized UOR activities exhibited by NNO2NO8 and NNO8NO2 reveal the importance of employing the generation of heterointerfaces as a strategy for boosting the electrocatalytic activity of Ni-based UOR catalysts with reduced Ni-mass loading; it is an effective strategy for designing high-active UOR catalysts, apart from the extensively employed approach of introducing high-valent or positively polarized Ni-centers.

The Tafel plot, wherein current density vs. the applied UOR potential is plotted, is imperative for gauging and comparing the kinetics of reactions mediated by electrocatalysts (Figure 3(e)). The Tafel slopes of the synthesized catalysts follow the order NNO2NO8 < NNO8NO2 < $NdNiO_3$ < NNO6NO4 < NNO4NO6 < NiO, which further highlights the superior UOR electrocatalytic kinetics exhibited by NNO2NO8 over the

other catalysts. Therefore, the greater number of NiOOH species, higher UOR current density, and lower Tafel slope substantiate the superior electrocatalytic behaviour of NNO2NO8 and NNO8NO2 catalysts over the other systems under study. A comparative analysis of the performance of the catalyst with reported hetero-junction/-interface/-structure catalysts is summarized in Table S3, presented in the supporting information.

The electrochemically-accessible surface area (ECSA) of the synthesized catalysts is calculated using the double-layer capacitance method and summarized in Figure S10 and Table S4. The ECSA increases gradually from NiO to NNO8NO2, after which it decreases in $NdNiO_3$. Perhaps this suggests that the stabilized Ni^{3+} ions of $NdNiO_3$ at the interface provide more charge carrier concentration than NiO-rich heterostructures (at double-layer regions), and these positive charges interact more with OH^- ions, resulting in the enhancement of C_{dl}. Although the stabilized Ni^{3+} ions provide more hole or positive ion concentration at the heterointerface, resulting in a higher C_{dl} value, they do not effectively provide active NiOOH species, which results in poor UOR activity [39]. As a consequence, there seems to be no direct relationship between the UOR activity and ECSA. For instance, NNO2NO8 (0.858 cm^2) has lower ECSA than NNO6NO4 (2.25 cm^2) and $NdNiO_3$ (1.45 cm^2), but the UOR activity follows the reverse trend.

The turnover frequency (TOF) of all the synthesized catalysts at various potentials is calculated from the number of loaded Ni-sites (Table S5 and Figure S11). The comparatively high TOF values of NNO8NO2 and NNO2NO8, when compared to the other catalysts and the individual components, highlight the high intrinsic activity of NNO8NO2 and NNO2NO8. However, the highest UOR activity in terms of current density was observed for NNO2NO8 with a catalyst loading amount of 0.04 mg of catalyst on 0.07 cm^2 electrode surface area (same for all the catalysts under study). This makes NNO2NO8 operationally more relevant than the other catalysts. To evaluate the selectivity of NNO2NO8 for UOR over the competing OER, step voltage analysis[40] and rotating ring disk electrode experiments (RRDE) are used [40–42]. Step voltage analysis (Figure S12 (a & b) reveals a current efficiency ranging from 97.7% to 99.3% for UOR. This agrees closely with the faradaic efficiency of 96.0% to 97.2% for UOR, as determined through RRDE experiments (Figure S12 (c & d)). This observation highlights the excellent selectivity of the optimized $NdNiO_3$-NiO catalyst, NNO2NO8 for UOR.

The stability of the most active UOR catalyst among the investigated catalysts, NNO2NO8, is studied by chronoamperometry (*i-t*) performed at 0.60 V vs. Hg/HgO for 48 h in 0.80 M U + 1 M KOH (Figure 3(f)). After the initial spike in current density, it stabilizes and retains 95% of the UOR current density by the end of 48 h of urea electrolysis. Further, the stability test is also conducted in two-electrode configuration with catalyst on Ni foam under stirred conditions for 100 h, and the amperometry *i-t* curve is presented in Figure S13.

The structure and morphology of the NNO2NO8 catalyst after subjecting to an *i-t* run are examined

employing XRD, FESEM, HRTEM, and XAS to monitor any changes in the catalyst (Figure S14). Post-mortem powder XRD analysis (Figure S14(a)) reveals that there is no apparent change in the bulk chemical structure of the initial catalyst after the stability test. However, the post-mortem TEM image (Figure S14(b)) indicates the formation of an amorphous layer, perhaps NiOOH, on the catalyst surface. Moreover, lattice fringes corresponding to a *d*-spacing of 0.233 nm corresponding to (101) planes of $Ni(OH)_2$ are observed, hinting towards the occurrence of the indirect mechanism of UOR, which is characterized by the formation of $Ni(OH)_2$ [31]. EDS mapping (Figure S14(c)) shows a uniform distribution of the constituent elements after the stability test. EDS analysis indicates a slight decrease in the atomic percentage of Nd in the catalyst after the stability test (Table S6), which could be attributed to catalyst reconstruction. From post-stability FESEM micrographs (Figure S14(d)), it can be observed that the irregular crystallites of NNO2NO8 contain loosely clumped masses, which could be formed due to catalyst reconstruction that occurs during the electrochemical process. The Ni K-edge XANES plot of NNO2NO8 before and after the stability test is shown in Figure S14(e). The edge position of Ni in NNO2NO8 shows a slight negative shift after the stability test, indicating a decrease in the average oxidation state of Ni, arising from the $Ni(OH)_2$ species formed from the *in-situ* generated NiOOH during UOR. Furthermore, the post-stability sample of NNO2NO8 demonstrates a decrease in the white-line intensity, perhaps occurring due to geometrical reconstruction or octahedral distortion that is also reported in other Ni-based anodic catalysts [31,43].

In situ Raman spectro-electrochemical experiments are employed to study the formation and fate of active species formed on the most active catalyst, NNO2NO8 (Figure S15 in supporting information) [44]. Figure S15(a) shows the *in-situ* Raman spectra of NNO2NO8 recorded in 1 M KOH under various anodic potentials. The activated NNO2NO8 showed two characteristic peaks of NiOOH at 476 cm^{-1} and 558 cm^{-1} corresponding to the E_g mode and A_{1g} mode, respectively, of the NiO_2 in NiOOH species [45], confirming the formation of NiOOH as the active species for UOR. The peaks remain prominent at all relevant anodic potentials (0.44 V to 0.68 V). However, when urea is added to the electrolyte (0.80 M U), the peaks corresponding to NiOOH disappear, and the Ni^{2+}-O peak (~502 cm^{-1}) becomes apparent up to a potential of 0.52 V (Figure S15(b)) [45]. This is due to the consumption of NiOOH species by virtue of the indirect mechanism of UOR, which leads to the reduction of NiOOH into $Ni(OH)_2$ during UOR. Above 0.52 V, the NiOOH peaks become more prominent, signifying the retention of NiOOH species at higher anodic potentials. To evaluate the ability of the $NdNiO_3$-NiO (NNO2NO8) catalyst to regenerate NiOOH species after prolonged electrolysis, *in situ* Raman spectra were acquired following an extended stability test of 15 h (Figure S15(c)). The retention of characteristic NiOOH peaks at potentials above 0.52 V vs. Hg/HgO confirms the capacity of the catalyst to continuously generate NiOOH species even after prolonged electrolysis.

3.3. *In situ* XANES experiments

In situ X-ray absorption near edge structure (XANES) is acquired in the fluorescence mode to study the changes in the local structure of the catalyst during the reaction [46]. The position of the absorption edge helps to monitor changes in the oxidation state of the absorbing atom; therefore, the change in the edge position of the synthesized catalysts is monitored under *in situ* conditions of electrolysis using the *in situ* XAS cell setup as illustrated in Figure 4(a). The integral method of calculation of the edge position is employed to obtain precise values since the change in edge positions is typically minute under operating conditions (Figure 4(e)).

According to the indirect mechanism of UOR, the electrochemically formed NiOOH species on the catalyst surface undergoes reduction to form $Ni(OH)_2$ during the oxidation of urea molecules, while during the direct mechanism of UOR, the electrochemically formed NiOOH species remain intact during urea electro-oxidation [38,47]. Therefore, for a Ni-based catalyst that follows the indirect

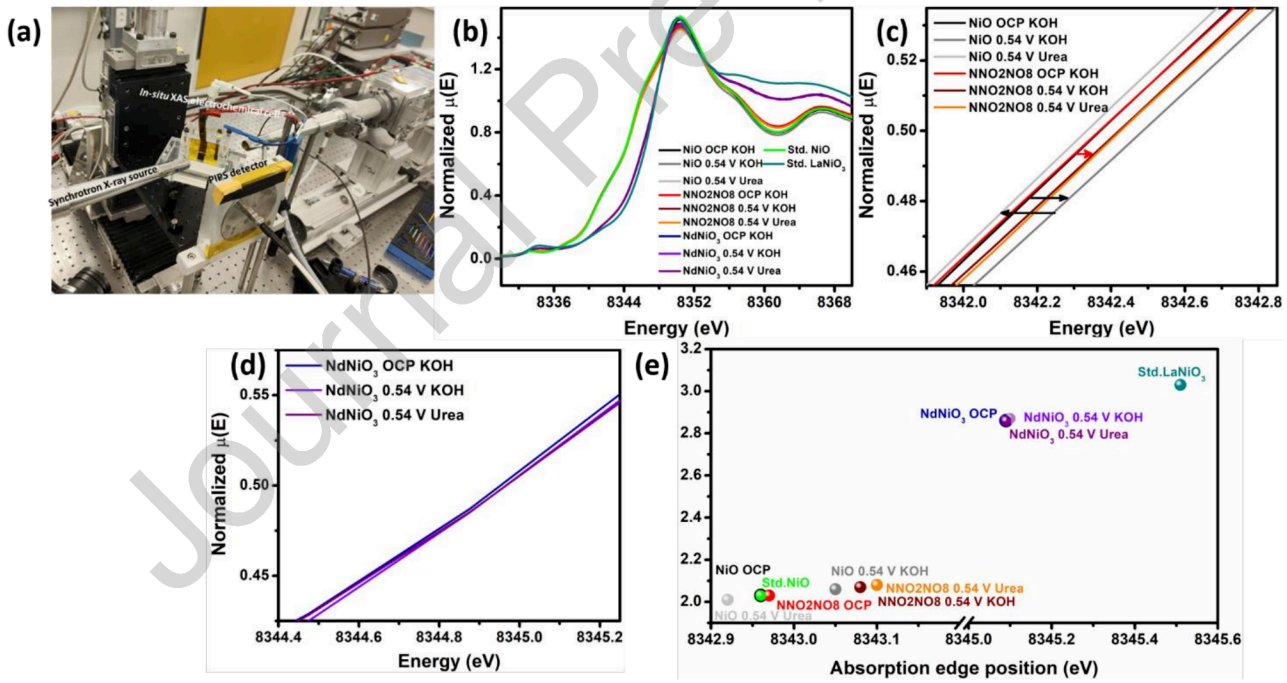

***Figure 4**. (a) Photograph of in situ XAS electrochemical setup, (b) Ni-K edge XANES of NiO, NNO2NO8 and $NdNiO_3$ acquired under in situ conditions, (c) Expanded view of in situ Ni-K edge XANES of NiO and NNO2NO8 (d) Expanded view of in situ Ni-K edge XANES $NdNiO_3$ (e) Plot of absorption edge position vs. oxidation state of Ni in the catalysts under in situ conditions.*

mechanism of UOR, the local average oxidation state of Ni is expected to remain close to +2 due to the rapid consumption of *in situ* generated-Ni^{3+} ions for the electrochemical oxidation of urea [37]. To evaluate the changes in oxidation states of Ni owing to the type of mechanisms operating in NiO, $NdNiO_3$ and the

optimized catalyst, NNO2NO8 during the electrochemical process, XAS spectra are acquired at open-circuit potential (OCP) in 1 M KOH, at 0.54 V vs. Hg/HgO in 1 M KOH, and at 0.54 V vs. Hg/HgO in urea-containing 1 M KOHelectrolyte (Figure 4(b)). The edge position of Ni in NiO has increased from 8342.96 eV at OCP to 8343.05 eV at 0.54 V in 1 M KOH, signifying an increase in the average oxidation state of Ni due to the formation of NiOOH species at the applied anodic potential. A similar shift in the edge position of Ni is observed in the case of NNO2NO8 [from 8342.97 eV (at OCP) to 8343.08 eV (at 0.54 V)] under applied anodic potential in 1 M KOH. However, when urea is added, the edge position of Ni in NiO dropped to 8342.92 eV due to the rapid consumption of NiOOH species through the indirect UOR mechanism, which results in a decrease in the average oxidation state of Ni (Figure 4(c)). In contrast to the negative edge position shift exhibited by NiO in the presence of urea, the XANES of NNO2NO8 retained its edge position at 8343.10 eV during UOR (at 0.54 V). The characteristic changes in the oxidation state of Ni calculated from the edge positions under *in situ* conditions are shown in Figure 4(e). In our previous work on the indirect UOR catalyst - $Ni_3O_2(OH)_4$, we have shown that a drop in the oxidation state of Ni in the presence of urea is a consequence of the poor active site regeneration capability of the UOR catalyst [48]. Conversely, the retention in the higher average oxidation state of Ni during UOR in NNO2NO8 could be due to the rapid regeneration of active NiOOH species that readily restores the electrocatalytic UOR activity of the catalyst. However, the XANES of $NdNiO_3$ (direct UOR catalyst) retains a high edge position of 8345.10 eV in 1 M KOH and in the presence of urea at 0.54 V vs. Hg/HgO, which, as shown in our previous work, is due to the predominant operation of direct UOR which retains NiOOH species (Figure 4(d)) [31].

3.4. Electrochemical Impedance Spectroscopy

The electrochemical impedance spectra of the catalysts recorded in 0.80 M U + 1 M KOH are carefully examined to draw conclusions about the electrochemical processes and mechanisms in these catalysts [49–52]. The plots of log frequency vs –phase angle, Bode plots, of all the catalysts under investigation are shown in Figure 5. The characteristic frequency response represents a distinct relaxation process and is thus useful for distinguishing various electrochemical processes occurring in the system [53]. The high-frequency response near $10^{2.5}$ Hz corresponds to the electrochemical interconversion of Ni^{2+}/Ni^{3+}, which happens during the NiOOH to $Ni(OH)_2$ reduction and re-oxidation due to the indirect UOR mechanism. The low-frequency relaxation process at a frequency range of $10^{1.7}$ to 10^{-1} Hz is attributed to the direct UOR mechanism, where electrons are transferred between the catalyst and urea, thereby oxidizing the latter.

Figures 5(a – f) present the Bode plots of all the $NdNiO_3$-NiO catalysts and the pristine components. As expected, NiO shows two distinct responses, one in the high-frequency region and another in the low-frequency, thereby indicating the co-existence of both the direct and indirect mechanisms of UOR (Figure

5(a)). In the case of $NdNiO_3$ (Figure 5(f)), the Bode plot shows a single response in the low-frequency region, corresponding to the direct UOR mechanism [31]. In NNO2NO8, the high-frequency response begins to diminish, suggesting the gradual predomination of the direct mechanism of UOR. The diminishing trend of the indirect mechanism is seen to get enhanced from NNO2NO8 to NNO8NO2, in agreement with the increasing percentage of $NdNiO_3$ component in these catalysts. (Figure 5(g)). This response almost completely disappears in NNO8NO2, thereby indicating that this catalyst possessing a higher percentage of $NdNiO_3$ (80%) drives UOR predominantly through the direct mechanism, with the slight inevitable operation of the indirect mechanism due to the presence of NiO.

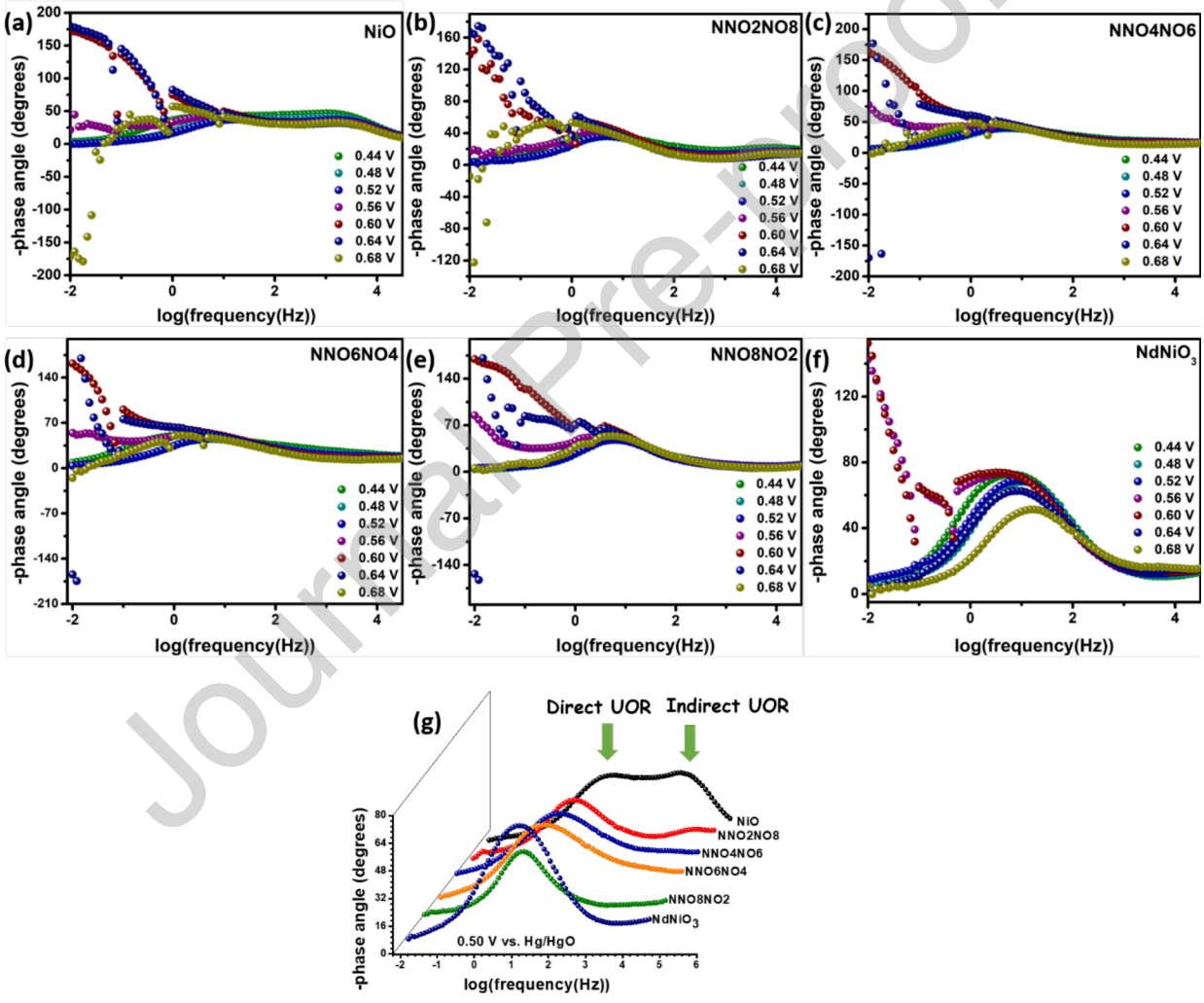

***Figure 5**. Bode plots of (a) NiO, (b) NNO2NO8, (c) NNO4NO6, (d) NNO6NO4, (e) NNO8NO2, (f) $NdNiO_3$ in 0.8 M U + 1 M KOH, (g) Bode plots of all the synthesized catalysts at 0.50 V vs. Hg/HgO in 0.8 M U + 1 M KOH.*

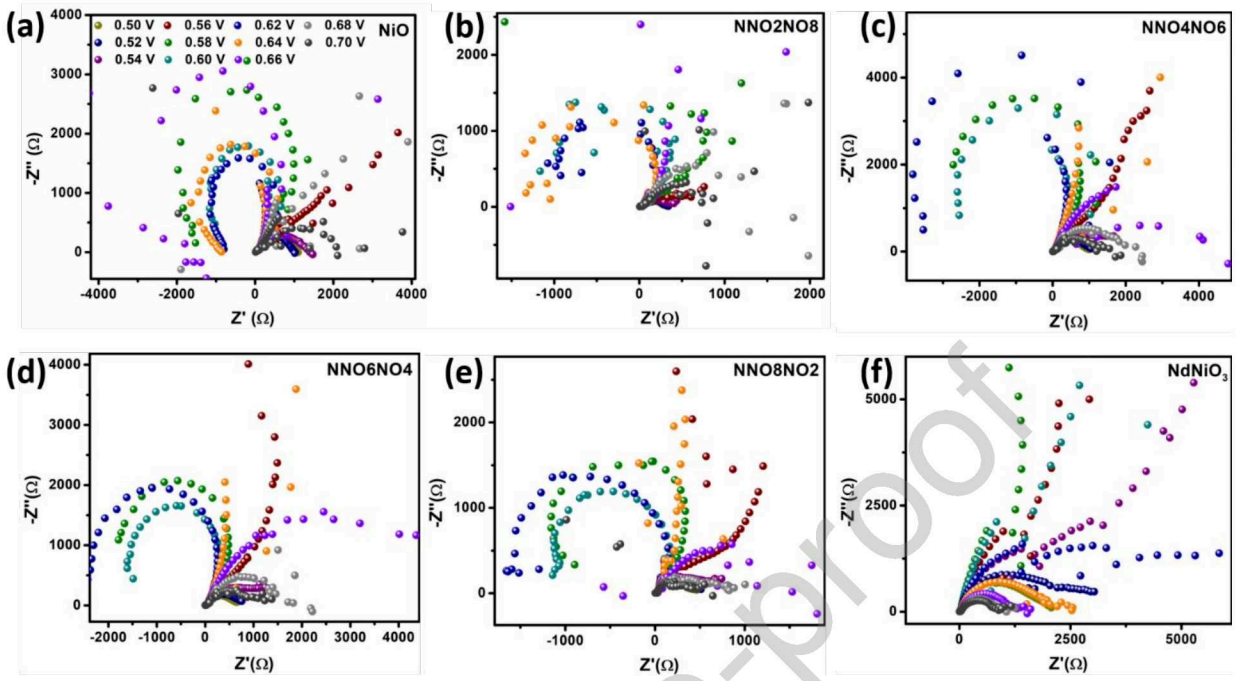

***Figure 6**. Nyquist plots of (a) NiO, (b) NNO2NO8, (c) NNO4NO6, (d) NNO6NO4, (e) NNO8NO2, (f) $NdNiO_3$ in 0.80 M U + 1 M KOH.*

The Nyquist plot, where the negative imaginary part of the impedance - *Z″*, is plotted against the real part of impedance *Z′* provides important information about electrode processes of UOR, such as the surface oscillatory phenomenon that is caused by CO_x poison accumulation (blockage of active sites) and its consequent removal by OH^- (revival of active site) [54]. The Nyquist plots of all the synthesized $NdNiO_3$-NiO catalyst systems at various UOR potentials are given in Figures 6 and S16. For NiO, a large semicircle is seen that results from the overlap of two broad semicircles as a consequence of the co-occurrence of the indirect and direct mechanisms of UOR also confirmed from the Bode plot (Figure 6(a) and Figure 5(a)). All the synthesized catalysts ranging from NNO2NO8 to NNO8NO2 also exhibit a large semicircle similar to NiO (Figure 6(b - e) & Figure S17), however with a gradually decreasing conspicuousness of the high-frequency semicircle that corresponds to the indirect mechanism of UOR (Ni^{3+} to Ni^{2+} interconversion). The Nyquist plot of $NdNiO_3$ (Figure 6(f)) comprises a single large semicircle that results from the occurrence of the direct mechanism of UOR. The noise-free impedance data points collected at potentials 0.46 and 0.48 V vs. Hg/HgO are fitted with the equivalent circuit(s) shown in Figure S17 and Table S7. The impedance data for NiO, NNO2NO8, NNO4NO6, NNO6NO4, and NNO8NO2 fit well with the typical UOR equivalent circuit [53]. The components of the typical UOR equivalent circuit include solution resistance (*Rs*), faradaic resistance (*R1*) and constant phase element (*CPE1*) corresponding to the indirect mechanism of UOR, and faradaic resistance (*R2*) and constant phase element (*CPE2*) corresponding to the direct mechanism of UOR. As expected, the direct UOR equivalent circuit with *Rs*, *R2* and *CPE2* was

sufficient to fit the impedance data points of $NdNiO_3$. This substantiates that NNO2NO8 exhibits both the direct and indirect mechanisms, but to an optimum extent to ensure sustenance of some amount of sturdy NiOOH species on the surface and simultaneously regenerate fresh NiOOH species from $Ni(OH)_2$ formed during the indirect UOR mechanism. The ability of NNO2NO8 to support both the direct mechanism due to inherently stabilized Ni^{3+} ions in $NdNiO_3$ and the indirect mechanism due to NiO, which contains predominantly Ni^{2+} ions, ensures the sustenance of NiOOH species on the surface, characteristic of the direct mechanism, while simultaneously regenerating fresh NiOOH from $Ni(OH)_2$ formed during the indirect mechanism. Perhaps the modulation of electronic structure in the heterointerfaces through electron transfer and charge redistribution between the constituent phases in the $NdNiO_3$-NiO catalysts (as elaborated later under theoretical analysis) enables the generation of sufficient NiOOH active species. This, consequently, may facilitate the rapid regeneration of consumed active sites, thereby enhancing the UOR activity and stability of catalysts that contain an abundance of these heterointerfaces.

It is well-established from previous works on UOR that the rate-determining step is CO_x production or desorption of intermediate CO_x [51,52,54]. The rate-determining step determines the position of the low-frequency impedance arc in the Nyquist plot. When the impedance arc lies in the first quadrant, i.e. when Z' is positive, it indicates that CO_x production is the rate-determining step of UOR. On the contrary, if the impedance arc is positioned in the second and higher quadrants with Z' bearing negative values due to electrochemical surface oscillation phenomena caused by CO_x surface poison accumulation and subsequent removal by OH^- ions, it can be concluded that CO_x desorption is the rate-determining step. At lower UOR potentials, the impedance arc is located in the first quadrant, signifying that CO_x production is the rate-determining step (r.d.s.). However, at higher anodic potentials, the impedance arc flips back into the first quadrant due to passivation of the catalyst surface by adsorbed OH^- ions, leading to the onset of OER. It can be observed from Figure 6(a - f), that the low-frequency Nyquist arcs of all the catalysts under investigation flip to the higher quadrants at different potential ranges; 0.58 to 0.70 V for NiO, 0.58 V to 0.68 V for NNO2NO8, 0.58 V – 0.64 V for NNO4NO6, 0.58 V to 0.64 V for NNO6NO4, 0.58 V to 0.68 V for NNO8NO2 and 0.56 V to 0.60 V for $NdNiO_3$ (vs. Hg/HgO) (Figure S18). Guo *et al.* in their work on Ni-Rh bimetallic dispersions suggested that a delay in the flipping of the Nyquist impedance arcs back into the first quadrant is a favorable attribute of a better UOR electrocatalyst [54]. They further explain that this delay occurring above the potential window wherein CO_x-desorption is the r.d.s. is due to an increased surface coverage by OH^- ions rather than urea, which leads to the predominant occurrence of OER over UOR. Therefore conceivably, the greater the delay (in terms of applied potential) in this flipping back of Nyquist arcs, the more effective will be the extent to which the UOR operates at those potentials. Therefore, the drawback of early onset of OER in $NdNiO_3$ is rectified by the $NdNiO_3$-NiO catalysts which are bestowed with a wider UOR operational potential window than $NdNiO_3$.

3.5. Theoretical Analysis

The theoretical analysis, using density functional theory (DFT), is conducted to elucidate the role of $NdNiO_3$-NiO heterointerfaces in enhancing urea oxidation reactions (UOR) by focusing on the adsorption behaviour of urea, OH^-, and CO_2. The exposed surface planes chosen for NiO and $NdNiO_3$ are (111) and (112), respectively, which are observed in XRD patterns. Top and side views of the $NdNiO_3$ and NiO planes are shown in Figure S19. The heterointerface of $NdNiO_3$-NiO was constructed by considering a rectangular supercell of Ni-terminated surface of NiO (11.81 Å ×10.22 Å) and the $NdNiO_3$ (7.61 Å × 10.76 Å). The optimized geometry of the hydroxylated heterointerface is represented in Figure 7. During optimization, the Nd atom from the $NdNiO_3$ surface forms bonds with the edge atoms (Ni & O) of the NiO surface. After hydroxylation, a slight distortion in the upper layer of the NiO surface is noticed, while the $NdNiO_3$ surface remains without any distortion. The NiO sublayer of $NdNiO_3$ surface maintains its continuity even after the heterointerface by bonding with the NiO sublayer of NiO surface.

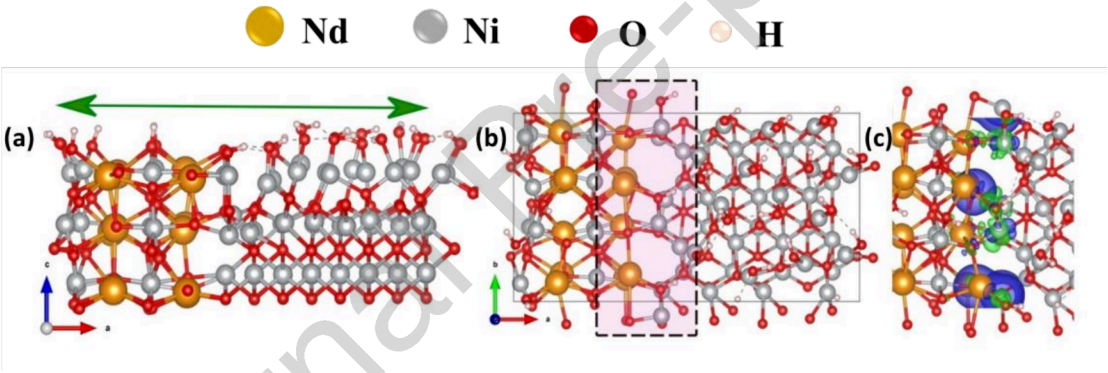

Figure 7*. The side view (a) and top view (b) of the optimized geometry of the heterointerface constructed with $NdNiO_3$ (112) and NiO (111) plane. The green arrow represents the length of the heterointerface, and the dotted rectangular region highlights the heterointerface region (c) The charge redistribution at the heterointerface. The green and blue colours indicate the accumulation and depletion of electrons, respectively.*

The $NdNiO_3$-NiO heterointerface exhibits an optimum work function of 4.59 eV compared to the individual surface planes of $NdNiO_3$ and NiO, (4.17 eV and 5.01 eV, respectively), which indicates possible electron transfer from lower to higher work function surface, i.e. from $NdNiO_3$ to NiO modulating the electronic structure at the heterointerface that could have a significant impact on the electrocatalytic properties of the catalyst (Table S9). The projected density of states (PDOS) at the heterointerface is computed and compared with those of the pristine NiO and $NdNiO_3$ surfaces, as shown in Figure S20 in the supporting information. It is evident from the PDOS plots that the valence region is primarily composed of Ni '*d*' orbitals and O '*p*' orbitals, while the conduction region involves contributions from O '*p*' orbitals, Ni '*d*' orbitals, and Nd '*d*' orbitals. The formation of the $NdNiO_3$-NiO heterointerface leads to an increased density of states near the

Fermi level, which facilitates charge transfer processes and plays a crucial role in enhancing the catalytic activity of the heterointerface [57]. Furthermore, Bader charge analysis reveals charge redistribution at the heterointerface, as illustrated in the optimized geometry of the $NdNiO_3$-NiO heterointerface in Figure 7(c). The Bader charge analysis conceivably implies polarization and charge redistribution at the heterointerface through electron accumulation and depletion that enhances the nucleophilic attack of OH^- ions during the oxy-hydroxylation process of generating the active NiOOH species [55]. In support of this argument, it is found that the adsorption energy for the OH^- species on $NdNiO_3$ and NiO is −1.31 eV and −0.79 eV, respectively, lesser than that of the heterointerface –2.01 eV, indicating stronger OH^- adsorption at the heterointerface of $NdNiO_3$-NiO. The surface of Ni-based catalysts is reconstructed into NiOOH by oxidation-hydroxylation in alkaline medium, under the influence of an applied anodic potential [58]. The enhanced ability of hydroxylation of $NdNiO_3$-NiO heterointerface due to improved adsorption of hydroxide ions on the catalyst surface could result in enhanced formation of UOR-active NiOOH species in the case of catalysts bearing an abundance of exposed $NdNiO_3$-NiO heterointerfaces.

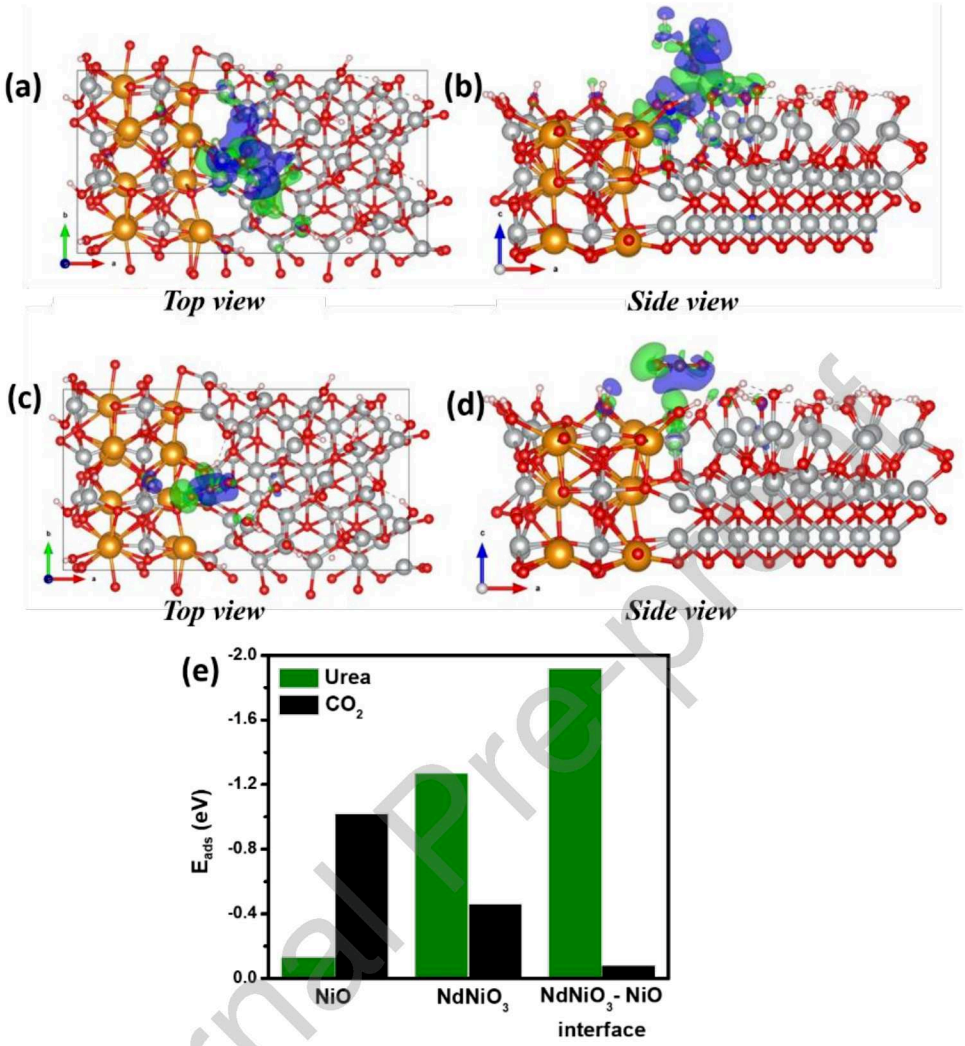

Figure 8*. The top and side views of charge density difference for the adsorption of (a) and (b) urea, and (c) and (d) CO_2 at the hydroxylated heterointerface. The green and blue colours indicate the accumulation and depletion of electrons, respectively, (e) Adsorption energies of hydroxylated $NdNiO_3$, NiO, and $NdNiO_3$-NiO heterointerface toward urea and CO_2.*

To initiate the urea oxidation reaction (UOR) on hydroxylated $NdNiO_3$-NiO heterointerfaces, the adsorption of urea is a crucial step. The higher the adsorption energy for urea, the greater will be the extent to which urea molecules will adsorb on the catalyst surface and undergo the subsequent oxidation process. According to density functional theory (DFT) calculations, the adsorption energy of urea on the hydroxylated $NdNiO_3$-NiO heterointerfaces is −1.92 eV, which is notably higher than that on the Ni-terminated $NdNiO_3$ (–1.27 eV) and NiO isolated surface (–0.13 eV) (Figure 8(a, b, and e) and Figure S22(a and c)). Perhaps the electron transfer at the heterogeneous interface generates built-in electric fields [33,59,60]. which could facilitate the targeted adsorption of urea molecules as reported in the case of $LaNiO_3$-NiO heterojunction

[22]. This phenomenon could bestow the $NdNiO_3$-NiO heterointerface with an enhanced ability to adsorb urea molecules, thereby resulting in enhanced UOR activity.

To provide a more comprehensive understanding of the thermodynamics of the intermediates formed during the urea oxidation reaction (UOR), the free energy changes associated with the typical UOR pathway [61,62] comprising key steps such as urea adsorption, dehydrogenation, C–N bond cleavage, CO oxidation, and CO_2 desorption is computed on the surface of hydroxylated heterointerface and presented in Table S8 and Figure S21 in the supporting information. Given the critical role of CO_2 desorption in UOR electrocatalysts, special emphasis has been laid on this step [6,31,51,63]. Efficient removal of CO_2 is essential to free the catalyst surface for the adsorption of new urea molecules, enabling sustained electrolysis. To assess this aspect, the adsorption energies of CO_2 were calculated for $NdNiO_3$, NiO and $NdNiO_3$-NiO heterointerface to identify the one that facilitates the most efficient desorption. The more negative adsorption energy of CO_2 signifies poor desorption of CO_2 from the catalyst surface. The calculated CO_2 adsorption energy for $NdNiO_3$ is –0.46 eV, and NiO is –1.02 eV, i.e. CO_2 desorption is more favourable in $NdNiO_3$ when compared to NiO. In the case of $NdNiO_3$-NiO heterointerface, the CO_2 adsorption energy is –0.08 eV, which is lower than that of the pristine components (Figure 8(c, d, & e) and Figure S22(b & d)). Additionally, from Bader charge analysis, it is calculated that 0.02|*e*| charge is transferred from the hydroxylated surface of $NdNiO_3$-NiO heterointerface to CO_2, while 0.05|*e*| and 0.14|*e*| charge is transferred in pristine $NdNiO_3$ and NiO, respectively (Figure S22 and Table S9). The minimal charge transfer and lower adsorption energy suggest the weaker binding of CO_2, which facilitates easy desorption of CO_2 from the heterointerface. This indicates that although all the synthesized catalysts undergo surface oscillations under applied UOR potential, caused by the two competing processes of the blockage of active sites by CO_x poisons and its subsequent removal by OH^- (as evidenced by impedance studies), the $NdNiO_3$-NiO catalysts that harbor the active heterointerfaces bestowed with favorable adsorption toward OH^- and desorption of CO_2, can demonstrate high CO_x poison tolerance which confers the catalyst with superior UOR activity and stability towards long-term electrolysis. Thus, the theoretical results provide important insights into the superior UOR activity of $NdNiO_3$-NiO catalysts. The stronger OH^- adsorption and more favourable urea adsorption at the heterointerfaces directly support the increased NiOOH formation and enhanced current densities observed in the experiments. Moreover, the calculated CO_2 adsorption energy at the heterointerface suggests weaker binding, which can explain the high tolerance to CO_x poisoning, conferring the catalyst with appreciable electrocatalytic stability.

4. Conclusions

In this work, we demonstrate the importance of the heterointerface that is formed between $NdNiO_3$ and NiO phases in $NdNiO_3$-NiO catalysts, and study the subsequent influence of the heterointerfaces on the UOR

activity. Although we could gradually tune the local average oxidation state of Ni by controlling the percentage ratio of $NdNiO_3$ and NiO, contrary to expectations, the oxidation state of Ni, the extent of NiOOH formation, and the UOR activity fail to follow a positive correlation. Furthermore, the content of NiO or $NdNiO_3$ does not directly correlate with NiOOH generation, UOR activity, or stability but instead influences the number of heterointerfaces formed in the $NdNiO_3$-NiO catalysts. The greater the number of heterointerfaces, the greater the ability to generate NiOOH species, which enhances the UOR output of the catalyst. Among the synthesized catalysts, the NNO2NO8 (20% $NdNiO_3$ and 80% NiO) and NNO8NO2 (80% $NdNiO_3$ and 20% NiO) pose excellent NiOOH formation feasibility, high UOR current density, mass activity, and low Tafel slope. This observation highlights the fact that the UOR activity in these catalysts stems majorly from the influence of the $NdNiO_3$-NiO heterointerfaces, regardless of changes in the local oxidation state. While *in situ* Raman spectroscopy provides compelling evidence for the formation and regeneration capability of UOR-active NiOOH species, *in situ* XAS and electrochemical impedance studies reveal the dynamic changes in these active species during UOR. Furthermore, results from theoretical calculations attribute the superior activity of the $NdNiO_3$-NiO catalysts, to the polarization and charge redistribution at the heterointerfaces.

In conclusion, this study highlights the importance of heterointerfaces as a key aspect for the feasible formation of active species and that enhancing the number and surface exposure of these heterointerfaces is an ideal catalyst design strategy to optimize UOR activity through synergistic effects and electronic structural modulation. The main challenge lies in synthesizing these catalysts to generate and expose a large number of active heterointerfaces on the surface, where the actual electrocatalytic process occurs.

CRediT authorship contribution statement

Nikhil N. Rao: Conceptualization, Methodology, Formal analysis, Investigation, Writing – original draft. **Chandraraj Alex:** Conceptualization, Methodology, Formal analysis, Investigation, Writing – review & editing. **Shalini Tomar:** Methodology, Formal analysis, Investigation, Writing – original draft **Muhammed Safeer N. K.:** Methodology, Investigation **Seung-Cheol Lee:** Methodology, Funding acquisition, Project administration **Satadeep Bhattacharjee:** Methodology, Investigation, Formal analysis, Writing: review & editing. **Neena S. John:** Supervision, Formal analysis, Funding acquisition, Project administration, Validation, Writing – review & editing.

Declaration of competing interest

The authors declare that they have no known competing interests that could have appeared to influence the work reported in this paper.

Acknowledgements

The authors thank SERB grant no. CRG/2022/006906 for funding. DST, India, is acknowledged for funding provided within the framework of the India@DESY program. DESY (Hamburg, Germany), a member of the Helmholtz Association HGF, is acknowledged for the provision of experimental facilities. Parts of this research were carried out at PETRA III beamline P64, and the authors would like to thank Dr. A. Kalinko for beamline guidance and Dr. M. Naumova for beamline assistance and useful discussions concerning XAS analysis. The authors acknowledge the Param Sanganak, IIT Kanpur supercomputing facility under the National Supercomputing Scheme (CDAC-NSM) for computing time. NNR thanks CeNS for the research fellowship. The authors also thank CRF, CeNS for characterization facilities.

REFERENCES

1. Ďurovič, M., Hnát, J., Bouzek, K., 2021. Electrocatalysts for the hydrogen evolution reaction in alkaline and neutral media. A comparative review. J. Power Sources 493, 229708. https://doi.org/10.1016/j.jpowsour.2021.229708.

2. Wang, T., Cao, X., Jiao, L., 2022. Progress in Hydrogen Production Coupled with Electrochemical Oxidation of Small Molecules. Angew. Chemie 134, e202213328. https://doi.org/10.1002/ange.202213328.

3. Arve, P.H., Popat, S.C., 2021. Stabilization of Urea for Recovery from Source-Separated Urine Using Electrochemically Synthesized Hydrogen Peroxide. ACS ES&T Eng. 1, 1642–1648. https://doi.org/10.1021/acsestengg.1c00194.

4. Boggs, B.K., King, R.L., Botte, G.G., 2009. Urea electrolysis: direct hydrogen production from urine. Chem. Commun. 4859. https://doi.org/10.1039/b905974a.

5. Ge, W., Lin, L., Wang, S.-Q., Wang, Y., Ma, X., An, Q., Zhao, L., 2023. Electrocatalytic urea oxidation: advances in mechanistic insights, nanocatalyst design, and applications. J. Mater. Chem. A 11, 15100–15121. https://doi.org/10.1039/D3TA02007J.

6. Daramola, D.A., Singh, D., Botte, G.G., 2010. Dissociation rates of urea in the presence of NiOOH catalyst: a DFT analysis. J. Phys. Chem. A 114, 11513–11521. https://doi.org/10.1021/jp105159t.

7. Zhu, D., Zhang, H., Miao, J., Hu, F., Wang, L., Tang, Y., Qiao, M., Guo, C., 2022. Strategies for designing more efficient electrocatalysts towards the urea oxidation reaction. J. Mater. Chem. A 10, 3296–3313. https://doi.org/10.1039/D1TA09989B.

8. Sun, W., Li, J., Gao, W., Kang, L., Lei, F., Xie, J., 2022. Recent advances in the pre-oxidation process in electrocatalytic urea oxidation reactions. Chem. Commun. 58, 2430–2442. https://doi.org/10.1039/D1CC06290E.

9. Lu, X.F., Zhang, S.L., Sim, W.L., Gao, S., Lou, X.W. (David), 2021. Phosphorized CoNi2 S4 Yolk-Shell Spheres for Highly Efficient Hydrogen Production via Water and Urea Electrolysis. Angew. Chem. Int.

Ed. Engl. 60, 22885–22891. https://doi.org/10.1002/anie.202108563.

10. Zhang, J., Zhu, J., Kang, L., Zhang, Q., Liu, L., Guo, F., Li, K., Feng, J., Xia, L., Lv, L., Zong, W., Shearing, P.R., Brett, D.J.L., Parkin, I.P., Song, X., Mai, L., He, G., 2023. Balancing dynamic evolution of active sites for urea oxidation in practical scenarios. Energy Environ. Sci. 16, 6015–6025. https://doi.org/10.1039/D3EE03258B.

11. Xie, J., Liu, W., Zhang, X., Guo, Y., Gao, L., Lei, F., Tang, B., Xie, Y., 2019. Constructing Hierarchical Wire-on-Sheet Nanoarrays in Phase-Regulated Cerium-Doped Nickel Hydroxide for Promoted Urea Electro-oxidation. ACS Mater. Lett. 1, 103–110. https://doi.org/10.1021/acsmaterialslett.9b00124.

12. Hao, P., Xin, Y., Wang, Q., Li, L., Zhao, Z., Wen, H., Xie, J., Cui, G., Tang, B., 2021. Lanthanum-incorporated β-Ni(OH)2 nanoarrays for robust urea electro-oxidation. Chem. Commun. 57, 2029–2032. https://doi.org/10.1039/D0CC07969C.

13. Liu, Y., Yang, Z., Zou, Y., Wang, S., He, J., 2024. Trace Cobalt Doping and Defect Engineering of High Surface Area α-Ni(OH)2 for Electrocatalytic Urea Oxidation. ENERGY Environ. Mater. 7, e12576. https://doi.org/10.1002/eem2.12576.

14. Cao, Q., Ye, Y., Sun, X., Liu, B., Lin, W., Ding, R., Gao, P., Liu, E., 2023. Boosting Urea Electrooxidation Activity of Ni5P4 by Vanadium Doping for Urea-Assisted Renewable Energy Conversion Devices. ACS Sustain. Chem. Eng. 11, 7136–7145. https://doi.org/10.1021/acssuschemeng.3c00398.

15. Maheskumar, V., Min, A., Moon, C.J., Senthil, R.A., Choi, M.Y., 2023. Modulating the Electronic Structure of Ni/NiO Nanocomposite with High-Valence Mo Doping for Energy-Saving Hydrogen Production via Boosting Urea Oxidation Kinetics. Small Struct. 4, 2300212. https://doi.org/10.1002/sstr.202300212.

16. Xu, S., Jiao, D., Ruan, X., Jin, Z., Qiu, Y., Feng, Z., Zheng, L., Fan, J., Zheng, W., Cui, X., 2024. O-2p Hybridization Enhanced Transformation of Active γ-NiOOH by Chromium Doping for Efficient Urea Oxidation Reaction. Adv. Funct. Mater. 34, 2401265. https://doi.org/10.1002/adfm.202401265.

italicized:

17. Wei, M., Zhang, D., Deng, J., Xiao, X., Wang, L., Wang, X., Song, M., Wang, S., Zheng, X., Liu, X., 2022. Cu-Doping Effect on the Electrocatalytic Properties of Self-Supported Cu-Doped Ni3S2 Nanosheets for Hydrogen Production via Efficient Urea Oxidation. Ind. Eng. Chem. Res. 61, 7777–7786. https://doi.org/10.1021/acs.iecr.2c00482.

18. Zhang, X., Fang, X., Zhu, K., Yuan, W., Jiang, T., Xue, H., Tian, J., 2022. Fe-doping induced electronic structure reconstruction in Ni-based metal-organic framework for improved energy-saving hydrogen production via urea degradation. J. Power Sources 520, 230882. https://doi.org/10.1016/j.jpowsour.2021.230882.

19. Duan, N., Hou, T., Zheng, W., Qu, Y., Wang, P., Yang, J., Yang, Y., Wang, D., Chen, J., Chen, Q., 2024. Insight into the Structure of Mn-NiS2 during Urea Oxidation Using Combined In Situ X-ray Absorption

Spectroscopy and Attenuated Total Reflectance Surface-Enhanced Infrared Absorption Spectroscopy. ACS Catal. 14, 1384–1393. https://doi.org/10.1021/acscatal.3c05369.

20. Wang, L., Zhu, Y., Wen, Y., Li, S., Cui, C., Ni, F., Liu, Y., Lin, H., Li, Y., Peng, H., Zhang, B., 2021. Regulating the Local Charge Distribution of Ni Active Sites for the Urea Oxidation Reaction. Angew. Chemie Int. Ed. 60, 10577–10582. https://doi.org/10.1002/anie.202100610.

21. Li, Z., Hu, M., Wang, P., Liu, J., Yao, J., Li, C., 2021. Heterojunction catalyst in electrocatalytic water splitting. Coord. Chem. Rev. 439, 213953. https://doi.org/10.1016/j.ccr.2021.213953.

22. Ding, H., Zhao, Z., Zeng, H., Li, X., Cui, K., Zhang, Y., Chang, X., 2024. Heterojunction-Induced Local Charge Redistribution Boosting Energy-Saving Hydrogen Production via Urea Electrolysis. ACS Mater. Lett. 6, 1029–1041. https://doi.org/10.1021/acsmaterialslett.3c01578.

23. Kang, B., Xu, B., Chen, Z., Li, F., Wang, Y., 2025. Promoting active hydrogen supply for kinetically matched tandem electrocatalytic nitrate reduction to ammonia. Appl. Catal. B Environ. Energy. 360, 124528. https://doi.org/10.1016/j.apcatb.2024.124528.

24. Chen, T., Wu, Q., Li, F., Zhong, R., Chen, Z., 2023. Co2P–Ni3S2 Heterostructured Nanocrystals as Catalysts for Urea Electrooxidation and Urea-Assisted Water Splitting. ACS Appl. Nano Mater. 6, 18364–18371. https://doi.org/10.1021/acsanm.3c03617.

25. Zhuo, X., Jiang, W., Yu, T., Qian, G., Chen, J., Yang, H., Yin, S., 2022. Crystalline–Amorphous Ni3S2–NiMoO4 Heterostructure for Durable Urea Electrolysis-Assisted Hydrogen Production at High Current Density. ACS Appl. Mater. Interfaces 14, 46481–46490. https://doi.org/10.1021/acsami.2c11238.

26. Guo, P., Cao, S., Huang, W., Lu, X., Chen, W., Zhang, Y., Wang, Y., Xin, X., Zou, R., Liu, S., Li, X., 2024. Heterojunction-Induced Rapid Transformation of Ni3+/Ni2+ Sites which Mediates Urea Oxidation for Energy-Efficient Hydrogen Production. Adv. Mater. 36, 2311766. https://doi.org/10.1002/adma.202311766.

27. Liu, J., Wang, Y., Liao, Y., Wu, C., Yan, Y., Xie, H., Chen, Y., 2021. Heterostructured Ni3S2–Ni3P/NF as a Bifunctional Catalyst for Overall Urea–Water Electrolysis for Hydrogen Generation. ACS Appl. Mater. Interfaces 13, 26948–26959. https://doi.org/10.1021/acsami.1c04325.

28. Wang, K., Huang, W., Cao, Q., Zhao, Y., Sun, X., Ding, R., Lin, W., Liu, E., Gao, P., 2022. Engineering NiF3/Ni2P heterojunction as efficient electrocatalysts for urea oxidation and splitting. Chem. Eng. J. 427, 130865. https://doi.org/10.1016/j.cej.2021.130865.

29. Xu, X., Liao, H., Huang, L., Chen, S., Wang, R., Wu, S., Wu, Y., Sun, Z., Huang, H., 2024. Surface reconstruction and directed electron transport in NiSe2/MoSe2 Mott-Schottky heterojunction catalysts promote urea-assisted water splitting. Appl. Catal. B Environ. 341, 123312. https://doi.org/10.1016/j.apcatb.2023.123312.

30. Zhang, Y., Lei, Y., Yan, Y., Cai, W., Huang, J., Lai, Y., Lin, Z., 2024. Enhancing hydrogen production capability from urine-containing sewage through optimization of urea oxidation pathways. Appl. Catal. B

Environ. Energy. 353, 124064. https://doi.org/10.1016/j.apcatb.2024.124064.

31. Rao, N.N., Alex, C., Mukherjee, M., Roy, S., Tayal, A., Datta, A., John, N.S., 2024. Evidence for Exclusive Direct Mechanism of Urea Electro-Oxidation Driven by In Situ-Generated Resilient Active Species on a Rare-Earth Nickelate. ACS Catal. 14, 981–993. https://doi.org/10.1021/acscatal.3c04967.

32. Caliebe, W.A., Murzin, V., Kalinko, A., Görlitz, M., 2019. High-flux XAFS-beamline P64 at PETRA III. In: AIP Conf. Proc., American Institute of Physics Inc., p. 060031. https://doi.org/10.1063/1.5084662.

33. Xie, Y., Feng, Y., Zhu, S., Yu, Y., Bao, H., Liu, Q., Luo, F., Yang, Z., 2024. Modulation in Spin State of Co3O4 Decorated Fe Single Atom Enables a Superior Rechargeable Zinc-Air Battery Performance. Adv. Mater. 2414801. https://doi.org/10.1002/adma.202414801.

34. Peck, M.A., Langell, M.A., 2012. Comparison of Nanoscaled and Bulk NiO Structural and Environmental Characteristics by XRD, XAFS, and XPS. Chem. Mater. 24, 4483–4490. https://doi.org/10.1021/cm300739y.

35. Qiu, Y., Gao, R., Yang, W., Huang, L., Mao, Q., Yang, J., Sun, L., Hu, Z., Liu, X., 2020. Understanding the Enhancement Mechanism of A-Site-Deficient LaxNiO3 as an Oxygen Redox Catalyst. Chem. Mater. 32, 1864–1875. https://doi.org/10.1021/acs.chemmater.9b04287.

36. Blume, A.R., Calvet, W., Ghafari, A., Mayer, T., Knop-Gericke, A., Schlögl, R., 2023. Structural and chemical properties of NiOx thin films: the role of oxygen vacancies in NiOOH formation in a H2O atmosphere. Phys. Chem. Chem. Phys. 25, 25552–25565. https://doi.org/10.1039/D3CP02047A.

37. R. Lin, L. Kang, T. Zhao, J. Feng, V. Celorrio, G. Zhang, G. Cibin, A. Kucernak, D.J.L. Brett, F. Corà, I.P. Parkin, G. He, Identification and manipulation of dynamic active site deficiency-induced competing reactions in electrocatalytic oxidation processes, Energy Environ. Sci. 15 (2022) 2386–2396. https://doi.org/10.1039/D1EE03522C.

38. V. Vedharathinam, G.G. Botte, Understanding the electro-catalytic oxidation mechanism of urea on nickel electrodes in alkaline medium, Electrochim. Acta. 81 (2012) 292–300. https://doi.org/10.1016/j.electacta.2012.07.007.

39. X. Liu, Z.Y. Zhai, Z. Chen, L.Z. Zhang, X.F. Zhao, F.Z. Si, J.H. Li, Engineering mesoporous NiO with enriched electrophilic Ni3+ and O− toward efficient oxygen evolution, Catalysts. 8 (2018) 310. https://doi.org/10.3390/catal8080310.

40. M. Zeng, J. Wu, Z. Li, H. Wu, J. Wang, H. Wang, L. He, X. Yang, Interlayer Effect in NiCo Layered Double Hydroxide for Promoted Electrocatalytic Urea Oxidation, ACS Sustain. Chem. Eng. 7 (2019) 4777–4783. https://doi.org/10.1021/acssuschemeng.8b04953.

41. B. Malik, K. Vijaya Sankar, S.K.T. Aziz, S. Majumder, Y. Tsur, G.D. Nessim, Uncovering the Change in Catalytic Activity during Electro-oxidation of Urea: Answering Overisolation of the Relaxation Phenomenon, J. Phys. Chem. C. 125 (2021) 23126–23132. https://doi.org/10.1021/acs.jpcc.1c06059.

42. X. Gao, X. Bai, P. Wang, Y. Jiao, K. Davey, Y. Zheng, S.-Z. Qiao, Boosting urea electrooxidation on oxyanion-engineered nickel sites via inhibited water oxidation, Nat. Commun. 14 (2023) 5842. https://doi.org/10.1038/s41467-023-41588-w.

43. H. Wang, Y. Hsu, R. Chen, T. Chan, H.M. Chen, B. Liu, Ni3+-Induced Formation of Active NiOOH on the Spinel Ni–Co Oxide Surface for Efficient Oxygen Evolution Reaction, Adv. Energy Mater. 5 (2015) 1500091. https://doi.org/10.1002/aenm.201500091.

44. F. Luo, S. Pan, Y. Xie, C. Li, Y. Yu, Z. Yang, Atomically dispersed Ni electrocatalyst for superior urea-assisted water splitting, J. Energy Chem. 90 (2024) 1–6. https://doi.org/10.1016/j.jechem.2023.10.007.

45. B.J. Trześniewski, O. Diaz-Morales, D.A. Vermaas, A. Longo, W. Bras, M.T.M. Koper, W.A. Smith, In Situ Observation of Active Oxygen Species in Fe-Containing Ni-Based Oxygen Evolution Catalysts: The Effect of pH on Electrochemical Activity, J. Am. Chem. Soc. 137 (2015) 15112–15121. https://doi.org/10.1021/jacs.5b06814.

46. J.-W. Zhao, H. Zhang, C.-F. Li, X. Zhou, J.-Q. Wu, F. Zeng, J. Zhang, G.-R. Li, Key roles of surface Fe sites and Sr vacancies in the perovskite for an efficient oxygen evolution reaction via lattice oxygen oxidation, Energy Environ. Sci. 15 (2022) 3912–3922. https://doi.org/10.1039/D2EE00264G.

47. V. Vedharathinam, G.G. Botte, Direct evidence of the mechanism for the electro-oxidation of urea on Ni(OH)2 catalyst in alkaline medium, Electrochim. Acta. 108 (2013) 660–665. https://doi.org/10.1016/j.electacta.2013.06.137.

48. M.S. Naduvil Kovilakath, C. Alex, N.N. Rao, D. Bagchi, A. Tayal, S.C. Peter, N.S. John, Unfolding the Significance of Regenerative Active Species in Nickel Hydroxide-Based Systems for Sustained Urea Electro-Oxidation, Chem. Mater. 36 (2024) 5343–5355. https://doi.org/10.1021/acs.chemmater.3c03062.

49. F. Guo, K. Ye, K. Cheng, G. Wang, D. Cao, Preparation of nickel nanowire arrays electrode for urea electro-oxidation in alkaline medium, J. Power Sources. 278 (2015) 562–568. https://doi.org/10.1016/j.jpowsour.2014.12.125.

50. S.N. Wu, Y.F. Qi, Q. Wang, X.G. Wang, X.J. Zhao, E.C. Yang, Nickel Foam-Supported Amorphous FeCo(Mn)−O Nanoclusters with Abundant Oxygen Vacancies through Selective Dealloying for Efficient Electrocatalytic Oxygen Evolution, ChemElectroChem. 7 (2020) 684–690. https://doi.org/10.1002/celc.201902070.

51. M. Safeer N. K., C. Alex, R. Jana, A. Datta, N.S. John, Remarkable COx tolerance of Ni3+ active species in a Ni2O3 catalyst for sustained electrochemical urea oxidation, J. Mater. Chem. A. 10 (2022) 4209–4221. https://doi.org/10.1039/D1TA05753G.

52. F. Guo, K. Ye, M. Du, X. Huang, K. Cheng, G. Wang, D. Cao, Electrochemical impedance analysis of urea electro-oxidation mechanism on nickel catalyst in alkaline medium, Electrochim. Acta. 210 (2016) 474–482. https://doi.org/10.1016/j.electacta.2016.05.149.

53. I.M.A. Mohamed, P. Kanagaraj, A.S. Yasin, W. Iqbal, C. Liu, Electrochemical impedance investigation of urea oxidation in alkaline media based on electrospun nanofibers towards the technology of direct-urea fuel cells, J. Alloys Compd. 816 (2020) 152513. https://doi.org/10.1016/j.jallcom.2019.152513.

54. S. Qian, Z. Rao, Y. Liu, J. Yan, B. Fan, Y. Gui, F. Guo, Nickel-Rhodium bimetallic dispersions supported on nickel foam as the efficient catalyst for urea electrooxidation in alkaline medium, Electrochim. Acta. 330 (2020) 135211. https://doi.org/10.1016/j.electacta.2019.135211.

55. S. Lu, M. Hummel, S. Kang, R. Pathak, W. He, X. Qi, Z. Gu, Density Functional Theory Investigation of the NiO@Graphene Composite as a Urea Oxidation Catalyst in the Alkaline Electrolyte, ACS Omega. 6 (2021) 14648–14654. https://doi.org/10.1021/acsomega.1c01758.

56. K. Peng, N. Bhuvanendran, F. Qiao, G. Lei, S.Y. Lee, H. Su, Coupling NiMn-Layered Double Hydroxide Nanosheets with NiCo2S4 Arrays as a Heterostructure Catalyst to Accelerate the Urea Oxidation Reaction, ACS Appl. Nano Mater. 6 (2023) 18318–18327. https://doi.org/10.1021/acsanm.3c03594.

57. C. Hu, K. Chu, Y. Zhao, W.Y. Teoh, Efficient Photoelectrochemical Water Splitting over Anodized p-Type NiO Porous Films, ACS Appl. Mater. Interfaces. 6 (2014) 18558–18568. https://doi.org/10.1021/am507138b.

58. L. Zheng, H. Luo, Y. Zhong, W. Li, H. Xu, F. Xiong, J. Pi, Y. Qing, Y. Wu, Wood-derived continuously oriented channels coupled with tunable built-in electric fields for efficient oxygen evolution, Appl. Catal. B Environ. Energy. 360 (2025) 124550. https://doi.org/10.1016/j.apcatb.2024.124550.

59. J. Liu, B. Zhang, P. Jian, J. Shi, Experimental and Theoretical Investigation of Interfacial Engineering in Fe2O3/NiFe2O4 Heterostructures toward the Cycloaddition of CO2 with Styrene Oxide., Inorg. Chem. 63 (2024) 12981–12991. https://doi.org/10.1021/acs.inorgchem.4c01696.

60. X. Xu, X. Wei, L. Xu, M. Huang, A. Toghan, Elucidating the promotion mechanism of the ternary cooperative heterostructure toward industrial-level urea oxidation catalysis, J. Energy Chem. 85 (2023) 116–125. https://doi.org/10.1016/j.jechem.2023.05.012.

61. S.W. Tatarchuk, R.M. Choueiri, A.J. MacKay, S.J. Johnston, W.M. Cooper, K.S. Snyder, J.J. Medvedev, A. Klinkova, L.D. Chen, Understanding the Mechanism of Urea Oxidation from First-Principles Calculations, ChemPhysChem. 25 (2024) e202300889. https://doi.org/10.1002/cphc.202300889.

62. S. Lu, M. Hummel, Z. Gu, Y. Wang, K. Wang, R. Pathak, Y. Zhou, H. Jia, X. Qi, X. Zhao, B. Bin Xu, X. Liu, Highly Efficient Urea Oxidation via Nesting Nano-Nickel Oxide in Eggshell Membrane-Derived Carbon, ACS Sustain. Chem. Eng. 9 (2021) 1703–1713. https://doi.org/10.1021/acssuschemeng.0c07614.

63. X. Zhu, X. Dou, J. Dai, X. An, Y. Guo, L. Zhang, S. Tao, J. Zhao, W. Chu, X.C. Zeng, C. Wu, Y. Xie, Metallic Nickel Hydroxide Nanosheets Give Superior Electrocatalytic Oxidation of Urea for Fuel Cells, Angew. Chemie - Int. Ed. 55 (2016) 12465–12469. https://doi.org/10.1002/anie.201606313.

Declaration of interests

☒ The authors declare that they have no known competing financial interests or personal relationships that could have appeared to influence the work reported in this paper.

☐ The authors declare the following financial interests/personal relationships which may be considered as potential competing interests:

Graphical abstract

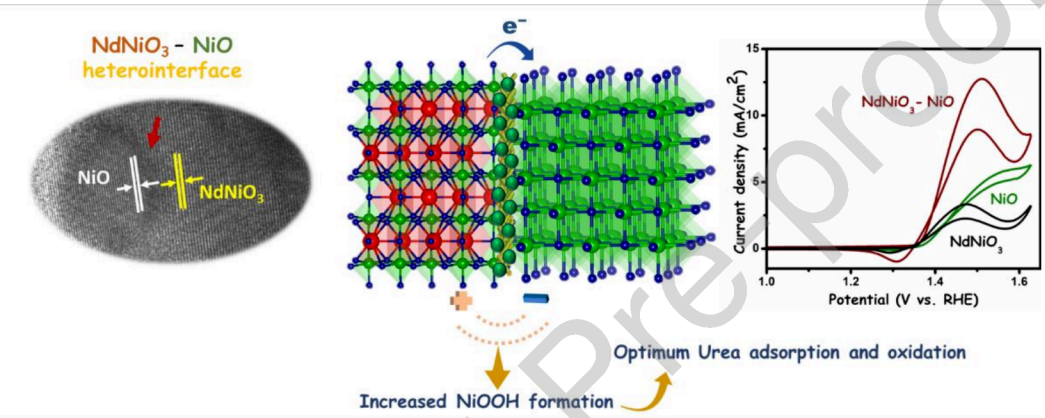

Highlights

- $NdNiO_3$-NiO with various stoichiometric ratios and the effect of Ni oxidation state on UOR.
- $NdNiO_3$-NiO heterointerfaces as ideal sites for UOR-active NiOOH formation.
- Operating UOR mechanism is governed by the proportion of $NdNiO_3$ to NiO.
- Optimum hydroxylation, urea adsorption, and CO_2 desorption at the heterointerfaces.